Centro de Investigación y de Estudios Avanzados
del Instituto Politécnico Nacional

Unidad Mérida

Departamento de Física Aplicada

"Simulaciones de la fuente de calor adicional debida a la nube de electrones para las secciones de arco del Gran Colisionador de Hadrones y comparación con mediciones criogénicas"

Tesis que presenta

Georfrey Humberto Israel Maury Cuna

para obtener el Grado de

Doctor en Ciencias

en la Especialidad de

Física Aplicada

Directores de la Tesis

Dr. Frank Zimmermann

Dr. Jesús Guillermo Contreras Nuño

Mérida, Yucatán, México **September, 2013**

CERN-THESIS-2013-496
06/09/2013

Centro de Investigación y de Estudios Avanzados
del Instituto Politécnico Nacional

Unidad Mérida

Departamento de Física Aplicada

"Simulations of electron-cloud heat load for the cold arcs of the CERN Large Hadron Collider and comparison with measured data"

Tesis que presenta

Georfrey Humberto Israel Maury Cuna

para obtener el Grado de

Doctor en Ciencias

en la Especialidad de

Física Aplicada

Directores de la Tesis

Dr. Frank Zimmermann

Dr. Jesús Guillermo Contreras Nuño

Mérida, Yucatán, México **September, 2013**

Resumen

El Gran Colisionador de Hadrones (LHC, por sus siglas en inglés) de la Organización Europea para la Investigación Nuclear se ha convertido en una máquina exitosa que ha permitido importantes descubrimientos como el del 4 de julio de 2012, cuando fue anunciado el descubrimiento de una nueva partícula que es compatible con el bosón de Higgs. Dicho descubrimiento fue posible gracias al buen desempeño del acelerador. Sin embargo, una nube de electrones y sus efectos relacionados han sido detectados en el LHC. Dichos efectos, han mostrado ser un problema fundamental para el buen desempeño de la máquina; además, constituyen una limitante para alcanzar los parámetros nominales de diseño del LHC. Dentro de la cámara de vacío del Colisionador se forma una nube de electrones ya sea por ionización del gas residual o por fotoemisión cuando la radiación sincrotrón del haz de partículas interacciona con las paredes metálicas de la cámara de vació. Esta colección de electrones va en aumento can cada paso de los paquetes de partículas al ser acelerados. Una preocupación vital para la seguridad del LHC es la fuente de calentamiento adicional debida a la nube de electrones que es capaz de sobrepasar los límites de la capacidad criogénica de enfriamiento y provocar una pérdida del estado superconductor de los magnetos en los arcos de LHC. Esta tesis presenta los resultados obtenidos mediante simulaciones computacionales del efecto de la nube de electrones en el interior del colisionador. Se estudio el calentamiento adicional para las condiciones nominales de operación del LHC. Se incluye, también, una comparación entre mediciones criogénicas obtenidas de 2010 a 2012.

Abstract

The CERN Large Hadron Collider (LHC) has become a very successful discovery machine. On 4 July 2012 the discovery of a new particle was announced, a candidate to be the famous Higgs boson. This extraordinary discovery was possible due to the excellent performance of the machine. However, an electron cloud and related effects have been detected in the LHC and have proven to be a problem for the optimal performance of the LHC and a limitation to reach its nominal design operation. Inside the LHC vacuum chamber, either by ionization of residual gas or photoemission due to the beam synchrotron radiation, a collection of electrons are created and after amplification via secondary emission a substantial electron cloud may be generated along with its undesirable effects. A large concern, for the safe LHC operation is the additional heat load due to the electron cloud because it can overcome the limited cooling capacity and provoke a loss of the superconducting state in the bending magnets of the cold arcs of the LHC (a so-called "quench"). This thesis presents simulations of the electron-cloud heat load in the LHC. I discuss the heat load for the nominal design operation parameters. A comparison with measured data from 2010 to 2012 is also presented.

Acknowledgements

This thesis is the culmination of an adventure that began 4 years ago in September 2009, when I started my PhD. on particle accelerators physics. A great part of my PhD I spent it at the European Organization for Nuclear Research (CERN) where I had the opportunity to collaborate with an amazing group of people working together in synergy to commission and operate the most complex and expensive machine built so far: the Large Hadron Collider. I would like to say "thank you" to all the people at CERN who helped me with my research stay, especially Dr. Oliver Bruning, Dr. Massimo Giovanozzi, Dr. Gianluigi Arduini, Dr. Elias Metral, Dr. Giovanni Rumolo, M. Sc. Giovanni Iadarola and M. Sc. Octavio Dominguez for their useful help and support. Special thanks to my beloved friends Silvano Roubatel and Elizabeth Castaneda for their friendship, love and good moments we share together, without you my time in Switzerland would have been less enjoyable.

I would like to say "thank you" to my home institution CINVESTAV - Merida Campus for the great time I had studying and learning how to be a scientist. Especially to the professors: Dr. Juan José Alvarado Gil, Dr. Gerko Oskam, Dr. Francisco Carlos Larios Forte, Mrs. Heidy Miranda, Mrs. Maricarmen Iturralde and Miss Zhirnay Rodriguez for all their help and support during my studies.

Special thanks to my friend Dr. Mario Perez Cortes for his help and corrections to the present work.

To my family: Adriana, Juan, Jose and Rosario, thanks for all your love and support.

This work would not have been possible without the financial support I received from the Mexican National Council on Science and Technology (CONACYT), by the European Commission under the FP7 Research Infrastructures project EuCARD, Grant Agreement No. 227579 (EuCARD-AccNet), EPLANET project, CERN and CINVESTAV.

At last, but not the least this thesis was possible thanks to the help and support of two gentlemen who are a continuous source of inspiration to me: my thesis supervisors Dr. Jesús Guillermo Contreras Nuño and Dr. Frank Zimmermann. It is thanks to both of you that I have finished this project. I learnt a lot from both of you. I will always take into account your advice and wisdom in my future professional career. In particular, I would like to thank you for all the freedom and liberty you always granted to me, that is for me the most valuable gift.

Muchas gracias Silvano por tu apoyo y paciencia.

À mon petit chat… sans toi cela n'aurait pas été possible.
Merci pour ton amour, ta patience et ton réconfort.

Contents

List of Figures

List of Tables

Chapter 1

The Large Hadron Collider

1.1 Introduction

The Large Hadron Collider (LHC) is the biggest accelerator ever constructed and the world's largest and most complex scientific instrument. The fundamental scientific purpose of which is to explore the inner structure of matter and the forces that govern its behavior. It is based at the European Organization for Nuclear Research (known as CERN) in the Northwest suburbs of Geneva on the Franco-Swiss border. Such a complex machine works properly thanks to the joined efforts of a multidisciplinary group of engineers and scientists that operate and resolve its problems. It is one of those problems the subject of this PhD thesis: the heat load due to the electron cloud in the LHC.

In the following sections, a general perspective of the principles that permit accelerating particles in the LHC and its main features will be presented.

1.2 Physical principles of operation

The force on a charged particle q with velocity $\mathbf{v}$ due to the presence of an electric field $\mathbf{E}$ and a magnetic field $\mathbf{B}$ is given by Lorentz force equation:

$$\mathbf{F} = (\mathbf{E} + \mathbf{v} \times \mathbf{B}). \tag{1.1}$$

Particles are accelerated by the electric field and the magnetic field is employed to change their trajectories. The energy gain of a particle by an electric field is:

$$\Delta E = \int_{s_1}^{s_2} \mathbf{F} \cdot \mathrm{d}\mathbf{s} = \int_{s_1}^{s_2} q\mathbf{E} \cdot \mathrm{d}\mathbf{s} = qV. \tag{1.2}$$

The particle beam is accelerated by an alternating electric field. Radio frequency power, at a frequency f_{rf} is employed to feed an RF cavity that creates an alternating electric field along the particle trajectory. In the case of the LHC, this cavity is quasi spherical with two apertures that permit particles to pass through. When this alternating field is zero, particles that are passing through will remain unaffected; otherwise they are accelerated or decelerated. Due to this method of acceleration the particle beam is not continuous but bunched, i.e., the beam particles travel together in packets called bunches. If the RF frequency is a multiple of the revolution frequency, then the particles always arrive at the same amplitude of electric field. For ultra-relativistic beams, earlier particles will see a higher field which increases their energy and brings them onto a longer orbit around the ring and makes them arrive later on the next revolution, while those that are later will see the opposite field and will come back earlier. This produces the bunched nature of particle beams in the LHC, i.e., a packet of particle forms around a so-called synchronous position, with the particles moving around this central point at the synchrotron frequency. By displacing the RF field slightly in time with respect to the bunch, all particles receive on average a positive kick and are accelerated [1].

1.3 Main features

The LHC is made of eight arcs and an equal number of straight sections (see Figure 1.1. The arcs of the LHC contain the dipole magnets, 154 in each arc. Two counter-rotating particle beams circulate inside two beam pipes and collide with each other at four interaction points (ATLAS, ALICE, CMS and LHCb). In order to guide the particles along the 27-km circumference dipole magnets are needed to bend the particle trajectories and quadrupole magnets are necessary to help focusing the beam. Each LHC arc contains 23 regular cells; each cell is made of 6 dipole magnets and two quadrupole magnets (see Fig. 1.2) to focus both planes (vertical and horizontal). In addition, there are small higher-order magnets: sextupoles and quadrupoles employed to correct the beam orbit. The position and array of the magnets is called the accelerator lattice and along with the strength of each magnet it determines the beam optics. Table 1.1 lists the main machine parameters. The beam parameters are given in Table 1.2. The transverse beam size along the ring is given by $\sigma = \sqrt{\varepsilon\beta}$. The rms emittance ε_x (and ε_y for the vertical plane) measures the area of the beam in phase space. $\beta_x(s)$ and $\beta_y(s)$ are called beta functions. For each plane, the beam size is proportional to the square root of the beta function. These functions vary according to the optics with the longitudinal coordinate s.

1.3.1 The LHC beam screen

The superconducting nature of the LHC magnets makes it very important to keep the heat sources under control. There are several sources of heating associated with the circulating proton beams. The four main sources for the LHC are

- synchrotron light radiated by the high energy circulating proton beams;
- energy loss by nuclear scattering of residual-gas molecules;

- energy dissipation by image currents;
- energy dissipated during the development of electron clouds.

In order to intercept and handle the aforementioned heat sources, it was necessary to come up with a device that shields the cold bore of the magnets from the beam induced heat loads: the beam screen, the purpose of which is prevent overheating of the bending magnets. Figure 1.3 shows a picture of the actual LHC beam screen. It is the beam screen surface where the secondary electron emission process happens and its inner volume where the electron cloud develops. A key element of the LHC beam pipe that helps to absorb an important amount of photons due to synchrotron radiation is the so-called sawtooth pattern, a structure designed to intercept the primary photons in the horizontal plane and to minimize the amount of reflected photons (A more detailed description of the features of sawtooth pattern can be found at [2]).

Table 1.1: LHC machine parameters

Parameter	Units	Injection	Collision
Ring circumference	m	26658.883	
Number of main dipoles		1232	
Length of main dipoles	m	14.3	
Field of main dipoles	T	0.535	8.33
Bending radius	m	2803.95	
Revolution frequency	kHz	11.245	
RF frequency	MHz	400.8	

Table 1.2: LHC beam parameters

Parameter	Units	Injection	Collision
Proton energy	GeV	450	7000
Relativistic gamma		479.6	7461
Number of particles per bunch		10^{11}	
Longitudinal emittance	eVs	1.0	2.5
Transverse normalized emittance	μmrad	3.5	3.75
RMS bunch length	cm	11.24	7.55
RMS beam size in arc	mm	1.19	0.3
Instantaneus power loss per proton	W	3.15×10^{-16}	1.84×10^{-11}
Energy loss per turn	eV	1.15×10^{-1}	6.71×10^{3}
Critical photon energy	eV	0.01	44.14

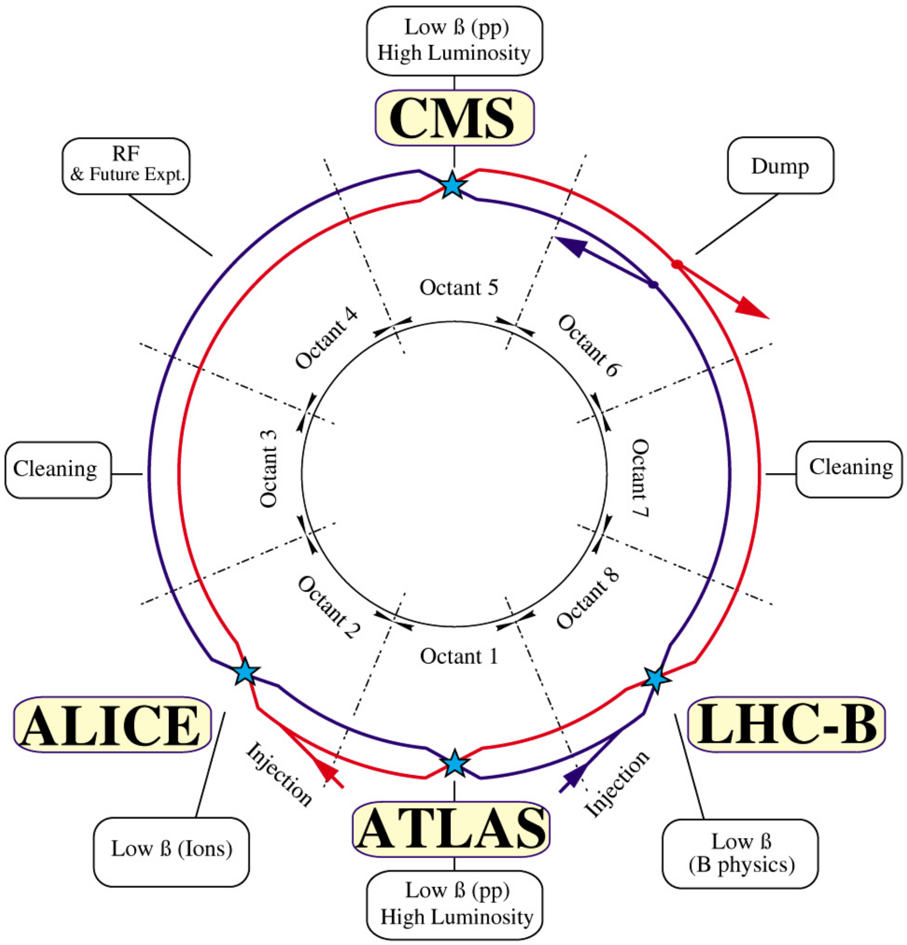

Figure 1.1: LHC general layout (*Courtesy of CERN).*

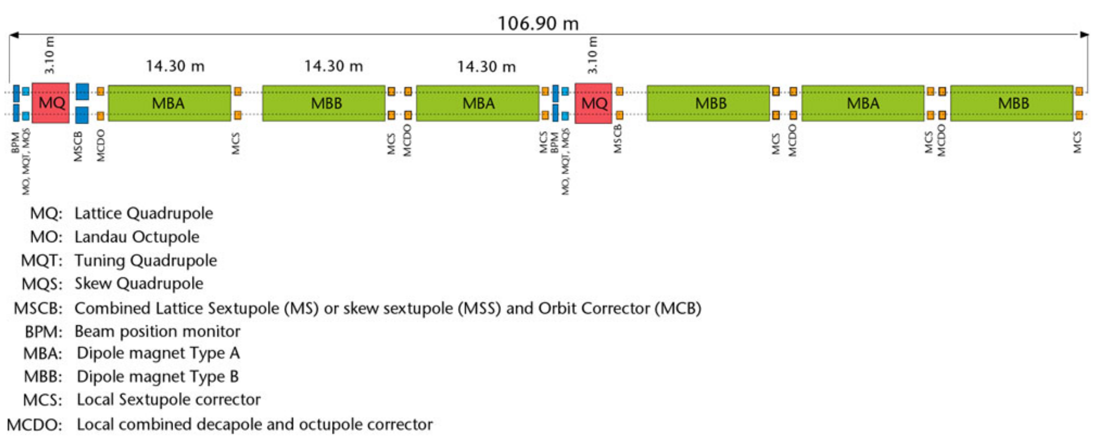

Figure 1.2: LHC arc cell schematic layout (*Courtesy of CERN).*

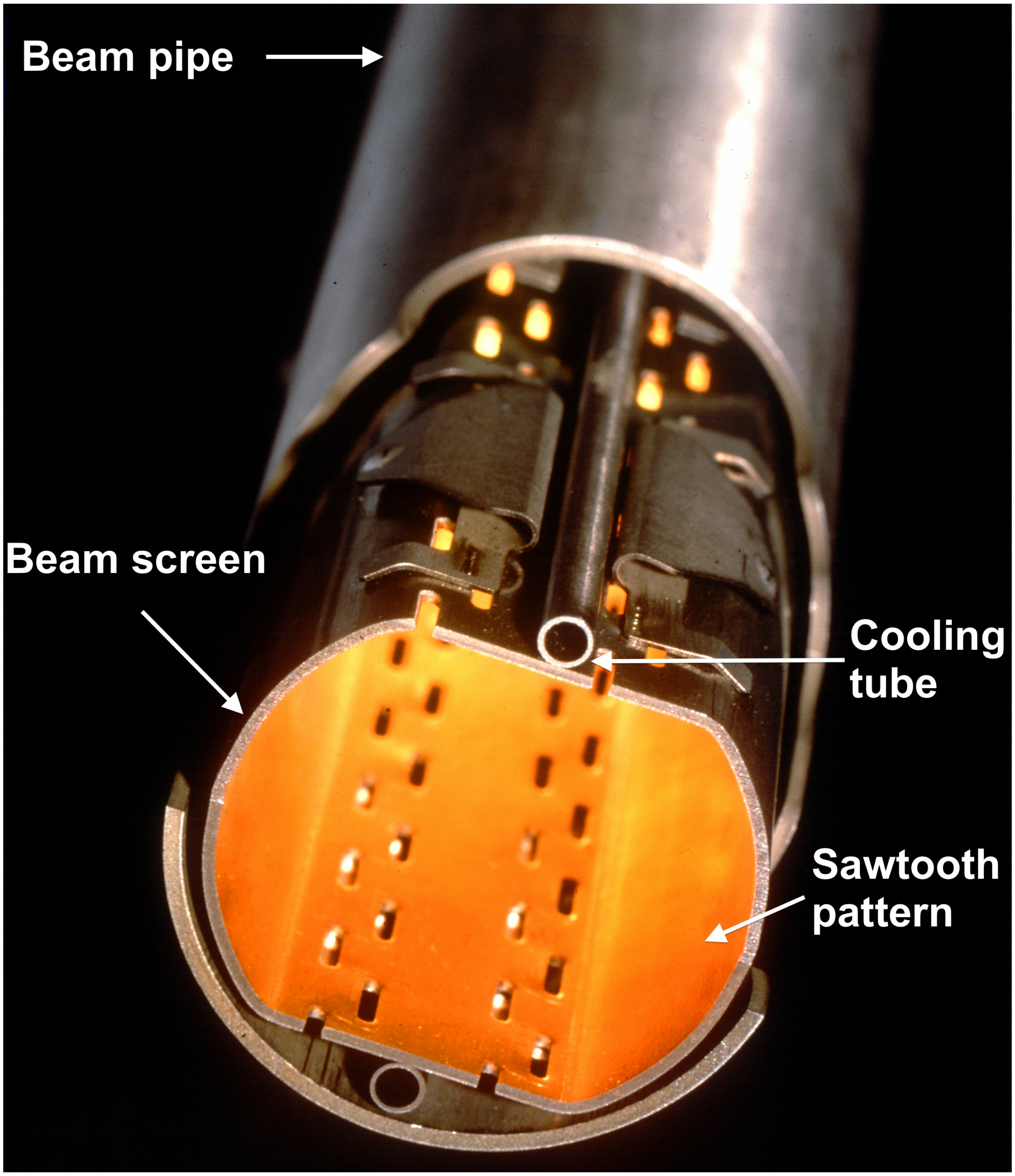

Figure 1.3: LHC beam screen (*Courtesy of CERN).*

Chapter 2

A Theoretical Analysis of Electron Cloud Build Up

2.1 Introduction

In the LHC, photoelectrons or secondary electrons generated on the wall during, or after, a bunch passage almost uniformly fill the vacuum chamber. When the next bunch arrives, it accelerates these electrons up to energies of several keV. This process repeats itself after each bunch passage and the result is a chain process where more and more electrons are being produced. The seed of the primary electrons can be by the photoelectric effect, when the synchrotron radiation from the proton beam hits the walls of the vacuum chamber or by residual-gas ionization. Whichever is the origin of the initial seed, the build-up of the electron cloud is a two-stage process: it starts with the production of primary electrons which can then generate one or several secondary electrons. Finally, after many bunch passages, the creation and recombination of electrons will reach an equilibrium state. This chapter is devoted to a theoretical analysis of the effects related to an electron cloud build up initiated either by synchrotron radiation or by residual gas ionization. Analytical treatments of the electron cloud effect were formulated throughout the past 20 years and the information presented here is based on the work of [3–7].

2.2 Photoemisison as a source of electron cloud

We will begin analysing the case when the primary seed is the photoelectrons from the beam-induced synchrotron radiation. The number of photons emitted by a bunch of charged particles in a bending magnetic field per unit time is

$$N_\gamma = \frac{5\alpha\gamma c N_b}{2\sqrt{3}\rho} \tag{2.1}$$

where α is the fine-structure constant, γ is the Lorentz factor, ρ is the bending radius, N_b is the number of particles per bunch, and c is the speed of light. For the nominal LHC proton energy of 7 TeV and nominal bunch intensity (1.15×10^{11} protons per bunch, Eq. 2.1 gives an amount about 9.75×10^{17} photons per second and per proton bunch. The critical energy of these photo-electrons is

$$E_{crit.} = \frac{3hc}{4\pi}\frac{\gamma^3}{\rho} = 44eV. \tag{2.2}$$

These photons after being emitted travel in synchronism with the bunch, and hit the wall, where they will produce the so-called photo-electrons.

2.3 Residual gas ionization as a source of electron cloud

at the LHC and its injector (SPS) it has been observed that ionization of the residual gas is also able to trigger the electron cloud effect.

Let us consider a gas with pressure P and with temperature T. On average, each gas molecule will occupy a volume V, according

$$PV = kT, \tag{2.3}$$

where k is the Boltzmann's constant. The average distance between the gas molecules is d_g

$$d_g = \left(\frac{kT}{P}\right)^{1/3}. \tag{2.4}$$

The probability that a proton hits a gas molecule will be inversely proportional to d_g^2, the number of hits per unit length is inversely proportional to d_g such that the average ionization rate per unit length and per proton is

$$r_{ion} = \sigma\frac{1}{d_g^3} = \sigma\frac{P}{kT}, \tag{2.5}$$

where the proportionality factor σ is the cross section associated with the ionization process. The cross section σ depends on the nature of the gas molecule and ranges from $1.8 \times 10^{-23}\mathrm{m}^2$ for H^2 and He to $13 \times 10^{-23}\mathrm{m}^2$ for CO_2 [8]. The initial seed of electrons per unit length and per bunch in the build-up process of the electron cloud is then

$$\left(\frac{dn_e}{ds}\right)_{init} = \sigma\frac{P}{kT}N_b, \tag{2.6}$$

where N_b is the number of protons per bunch.

2.4 Deflection of electrons by a passing bunch

If the one-dimensional longitudinal distribution function of the particles in the bunch is assumed to be Gaussian,

$$f_{part}(z,t) = \frac{N_b}{\sigma_z}\lambda\left(\frac{z-ct}{\sigma_z}\right), \tag{2.7}$$

where σ_z is the rms bunch length and the dimensionless function λ is

$$\lambda(\xi) = \frac{1}{\sqrt{2\pi}}e^{-\xi^2/2}, \tag{2.8}$$

the distribution of the photons from a single bunch hitting the wall per unit time per unit length and per unit azimuthal angle along the beam pipe cross section will be

$$n_\gamma(z,t,\phi) = \frac{N_\gamma G(\phi)}{\sigma_z}\lambda\left(\frac{z-ct}{\sigma_z}\right), \tag{2.9}$$

where $G(\phi)$ is a factor that gives the azimuthal distribution of the photons, such that $\int_0^{2\pi} G(\phi)\,\mathrm{d}\phi = 1$. Each photoelectron that is generated on the wall will be accelerated by the electric field of the passing bunch. In the kick approximation, which assumes that an electron does not change its radial position during the passage of the bunch, the energy of the photoelectron immediately after the passage is given by the following formula

$$\varepsilon(z,t,\phi) = \varepsilon P\left(\frac{z-ct}{\sigma_z}\right)^2 g(\phi)^2, \tag{2.10}$$

where

$$P(\xi) = \int_{-\infty}^{\xi}\lambda(x)\,\mathrm{d}x = \frac{1}{2}\left[1+\mathrm{erf}\left(\xi/\sqrt{2}\right)\right]. \tag{2.11}$$

The factor $g(\phi) = 1$ in magnetic field free regions; in dipoles where the strong vertical magnetic field constrains the electron motion to the vertical direction only, it is necessary to take a projection of the radial electric field of the beam on the vertical axis which results in $g(\phi) = \sin\phi$ (the angle ϕ is measured from the horizontal plane). For a given distribution of the photons on the wall, Eq. 2.9, and the energy gain for each electron given by Eq. 2.10,we can find the distribution function of the photoelectrons $f_{pe}(W,\phi)$ over the energy W and the azimuthal angle ϕ after the passage of the bunch:

$$f_{pe}(W,\phi) = Y^*\int_{-\infty}^{\infty}\delta[W-\varepsilon(z,t,\phi)]n_\gamma(z,t)\,\mathrm{d}t, \tag{2.12}$$

where Y^* is the photo-electron yield (number of electrons per absorbed photon) and δ in the integrand denotes the Dirac δ-function. The function $f_{pe}(W,\phi)$ is defined so that $f_{pe}(W,\phi)\,\mathrm{d}W\,\mathrm{d}\phi$ gives the number of photoelectrons left after the passage of the bunch per unit length of the beam pipe in the energy range $[W, W + \mathrm{d}W]$ within the azimuthal angle $[\phi, \phi + \mathrm{d}\phi]$. Performing the integration yields

$$f_{pe}(W, \phi) = \frac{Y^* N_\gamma}{4\pi c g(\phi)\sqrt{\varepsilon_{max} W}}. \tag{2.13}$$

The electron energy W in Eq. 2.13 varies from 0 to ε_{max} in the straight sections, and from 0 to $\varepsilon_{max}\sin^2\phi$ in dipoles.

2.5 Secondary electron production and model

A single electron that impinges on a surface will, on average, liberate a number of secondary electrons δ_{tot}. That number depends on the energy of the incoming electron and on the surface material. The material is characterized by its maximum yield δ^*_{max} and the energy ϵ^*_{max} where that maximum occurs. Photoelectrons will be accelerated by the beam. The energy of the second (and higher) generation electrons is determined by the beam properties. The distribution of secondary electrons has been approximated by a Maxwellian velocity distribution [9]. The secondary-emission yield δ_{tot} describes the average number of secondary electrons emitted per incident electron. It is a function of the energy of the primary incident electron and of its angle of incidence. The model used on this thesis, describes the total secondary-emission yield as the sum of a true secondary-electron component (δ_{true}) and an elastic reflection component (δ_{elast}):

$$\delta_{tot}(E_p, \theta) = \delta_{true}(E_p, \theta) + R\delta_{elast}(E_p), \tag{2.14}$$

where E_p is he incident-electron energy and θ the angle of incidence (with $\theta = 0$ referring to perpendicular impact). The coefficient R designates the probability for an elastic reflection in the limit of zero primary energy ($0 < R < 1$). We note that the true secondary yield is taken to depend on θ, while for the reflectivity part the approximation of being independent of θ is assumed (since no information about a θ-dependence is available).

The true secondary yield is parametrized as [10–12]

$$\delta_{true}(E_p, \theta) = \delta_{max}(\theta)\frac{\frac{sE_p}{\varepsilon_{max}(\theta)}}{s - 1 + \left[\frac{E_p}{\varepsilon_{max}(\theta)}\right]^s} \tag{2.15}$$

$$\delta_{max}(\theta) = \delta^*_{max} e^{\frac{1}{2}(1-\cos\theta)} \tag{2.16}$$

$$\varepsilon_{max}(\theta) = \varepsilon^*_{max}[1 + 0.7(1 - \cos\theta)] \tag{2.17}$$

with $s \approx 1.35$ (for fully conditioned copper [13]), and the elastic reflection as [14]

$$\delta_{elast}(E_p) = \left(\frac{\sqrt{E_p} - \sqrt{E_p + E_0}}{\sqrt{E_p} + \sqrt{E_p + E_0}} \right)^2, \tag{2.18}$$

with $E_0 = 150$ eV.

Figure 2.1 illustrates the secondary emission yield (δ_{tot} for angle of incidence $\theta = 0$. The maximum value of the curve corresponds to the coordinates: (δ^*_{max} and ε^*_{max}). At zero incident-electron energy the curve intercepts the y-axis at $(0, R)$.

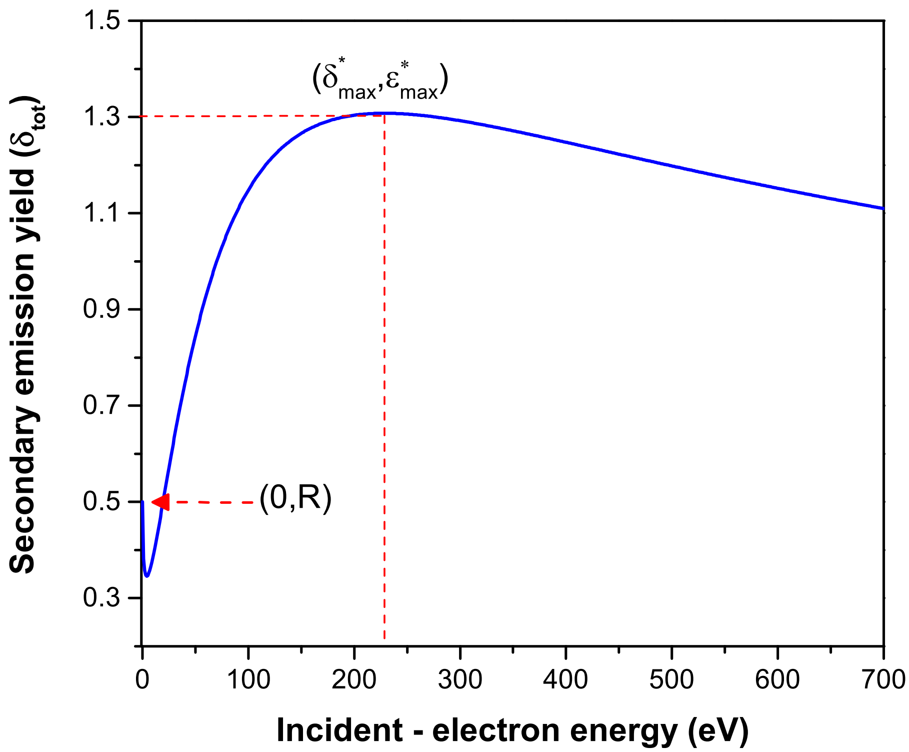

Figure 2.1: The secondary-emission yield δ_{tot} for perpendicular incidence, with $\delta^*_{max} = 1.3$ and $\varepsilon^*_{max} = 234.7$.

2.6 Multipacting

So far we have considered the electron cloud during the passage of a single bunch. Now we need to look at what happens with those electrons when subsequent bunches pass by. The generation of secondary electrons will occur rather uniformly in time between the first and the second bunch. After the second bunch arrives, it accelerates the secondary electrons up to an energy of several keV and causes them to hit the wall and to be converted into the next generation of secondaries almost immediately after the passage of the bunch. The same process repeats with the passage of next bunches. Let us set $t = 0$ to correspond to the moment immediately after the passage of the bunch under consideration. We assume that by this time all secondary electrons are produced and sit close to the wall surface. We also assume that their initial velocity distribution function is given by a half-Maxwellian with a characteristic energy W_s, and all electrons are emitted perpendicular to the wall surface. The total distribution function over velocity and coordinates at $t = 0$ is

$$f_e^0(\upsilon, x, y) = n_0(x)\sqrt{\frac{2m}{\pi W_s}} e^{-m\upsilon^2/2W_s}\delta[y - y_0(x)], \quad \upsilon > 0, \tag{2.19}$$

where the velocity υ is directed from the wall toward the axis, $y_0(x) = \pm\sqrt{x_0^2 - x^2}$ gives the y-coordinate of the wall for a given x, x_0 is the position on the wall and $n_0(x)$ is the number of electrons per unit area in the $x - z$ plane. The δ-function term reflects the fact that all electrons are initially localised on the wall. The function f_e^0 is defined so that when integrated over υ from 0 to infinity it gives the electron density (particles per cubic centimetre) in the pipe [$n_0(x)$ has a dimension of particles per unit area], and integrated over velocity and the geometrical cross section of the beam pipe, it gives the total number of the secondary electrons left after the passage of the bunch:

$$\int \mathrm{d}x\mathrm{d}y \int_0^\infty \mathrm{d}\upsilon f_e^0(\upsilon, x, y) = 2\int_{beam\ pipe} n_0(x)\mathrm{d}x = N_e. \tag{2.20}$$

In the case of a strong vertical magnetic field, we can assume that particles move only in the vertical direction, their horizontal position being "frozen" within a small Larmor radius. In order to compute the dynamics of the electron cloud, we actually need the distribution function over the vertical component of the velocity $\upsilon_y = \upsilon y_0/x_0$ which can be found from Eq. 2.19,

$$f_e^0(\upsilon_y, x, y) = \frac{2x_0 n_0(x)}{\upsilon_s y_0(x)}\lambda\left(\frac{\upsilon_y x_0}{\upsilon_s y_0(x)}\right)\delta[y - y_0(x)], \tag{2.21}$$

where $\upsilon_s = \sqrt{W_s/m}$ and λ is giving by Eq. 2.8.

In the course of the free motion of the electrons until the next bunch arrives, υ_y remains constant and $y = y_0(x) + \upsilon_y t$. Using the fact that the distribution function of a Hamiltonian system is a function of integrals of motion (and the Liouville theorem) we can easily find it from the one at time $t > 0$, according to

$$f_e(\upsilon_y, x, y, t) = f_e^0(\upsilon_y, x, y - \upsilon_y t). \tag{2.22}$$

Integrating this formula over υ_y gives the density of the electrons at time t,

$$n_e(x, y, t) = \frac{2x_0 n_0(x)}{t\upsilon_s y_0(x)}\left\{\lambda\left[\frac{y - y_0(x)}{t\upsilon_s y_0(x)}\right] + \lambda\left[\frac{y + y_0(x)}{t\upsilon_s y_0(x)}\right]\right\}. \tag{2.23}$$

The two terms in Eq. 2.23 account for the electrons that move along the field line from the upper and lower parts of the walls, respectively.

2.6.1 Acceleration of secondary electrons y the beam and multipacting condition

At time $t_{sep} = 25$ns the next bunch arrives (nominal bunch spacing for the LHC), and the secondary electrons distributed according to Eq. 2.23 get a kick from the electric field of this bunch. Accelerated up to energies of several keV they will quickly get to the walls and create a new generation of secondary electrons. If the number of new secondary electrons, $n_1(x)$, is larger than the initial number $n_0(x)$, we will have an exponential growth of the secondary electrons with the passages of subsequent bunches (in the absence of the space charge effect). In the opposite case, the initial group of photoelectrons will exponentially decay after several cycles. In order to find the threshold for multipacting we need to calculate the energies of the electrons which fill the beam pipe, after the passage of the next bunch, and find the corresponding number of the new generation of secondary electrons after they hit the wall. For this calculation, again we will assume a kick approximation for the energy gain. For an electron located at position x, y the kick energy gain is

$$W(x,y) = \varepsilon_{max} \frac{y^2 x_0^2}{(x^2+y^2)^2}. \tag{2.24}$$

In this expression we used the fact that the bunch electric field varies inversely proportional to the distance and included the projection of the electric field on the magnetic field line. Now it is possible to calculate the number of the new generation secondary electrons that are produced after the passage of the second bunch

$$n_1(x) = \int \mathrm{d}y \delta_{tot}[W(x,y), \theta] n_e(x,y,t_{sep}), \tag{2.25}$$

where t_{sep} is the time interval between bunches and the angle θ is related to x through $\cos\theta = y_0(x)/a$. As mentioned above, if the ratio $n_1(x)/n_0(x)$ is greater than 1, the multipacting occurs. Using Eq. 2.25, the condition for the multipacting can be written as

$$\delta_{max} > \delta_{crit}(x) = \left\{ \int \mathrm{d}y\, h[W(x,y)] \frac{x_0}{y_0(x)} \frac{n_e(x,y,t_{sep})}{n_0(x)} \right\}^{-1}. \tag{2.26}$$

2.7 Electron cloud build-up

Let us assume that the actual secondary emission yield is larger than the critical, $\delta_{max} > \delta_{crit}$. In this case, a group of electrons initially produced by a single bunch is amplified after each passage of subsequent bunches by a factor $1 + q$, where

$$q = |\delta_{max}/\delta_{crit} - 1|, \tag{2.27}$$

which means an exponential growth $N_e \approx N_{se} \exp(tq/t_{sep})$. In addition to amplifying the existing electron cloud, each bunch adds its own secondary electrons generated from photoelectrons. We can find the total density of the cloud after the passage of $M = t/t_{sep}$ bunches by summing the contributions from every bunch. Note that the electron density N_{se} generated by the kth bunch immediately after the passage by the time of observation will be amplified by a factor of $\exp[q(M-k)]$. The total density from all bunches is

$$N_e = \sum_{k=1}^{M} N_{se} e^{q(M-k)} = N_{se} \frac{e^{Mq} - 1}{e^q - 1} \approx \frac{N_{se}}{q} e^{tq/t_{sep}}, \tag{2.28}$$

where in the last formula we assumed that $q \ll 1$ and $Mq \gg 1$. Unlimited growth predicted by Eq. 2.28 will eventually be stopped by the space charge effect (see next section). If the multipacting condition is not satisfied, $\delta_{max} < \delta_{crit}$, then an initial electron cloud will decay as $N_{se} \approx \exp(-tq/t_{sep})$. Adding contributions to the cloud from other bunches results in a steady state density of the electron cloud at the level

$$N_e = \sum_{k=1}^{\infty} N_{se} e^{-qk} = N_{se} \frac{1}{e^q - 1} \approx \frac{N_{se}}{q}, \tag{2.29}$$

which means that for a small q there maybe a substantial increase in the electron density compared to the electron cloud for a single bunch. On the other hand, if the density given by Eq. 2.29 is so large that the space charge effects play a role, then it will actually limit the density before it reaches the equilibrium predicted by Eq. 2.29.

2.8 Space charge

The effect of space charge will eventually keep the build-up of the electron cloud within bounds. The build-up saturates when the repelling electron space charge on average neutralizes the field of the beam. The electric field of the space charge will effectively decelerate electrons when they are moving away from the wall toward the center, and push them back into the wall surface preventing the further build-up of the cloud. The inclusion of the space charge leads to a saturation of the electron-cloud density at a value close to the neutralization level, a condition that we define as

$$\lambda_e = \frac{N_b}{\Delta L_{sep}}, \tag{2.30}$$

where λ_e is the electron linear density and ΔL_{sep} the distance between adjacent bunches.

2.9 Synchronous phase shift due to the electron cloud

So far, we have investigated the electron cloud build-up from an analytical point of view. For the LHC, a way to get experimental information about the build-up is by measurements of the individual bunch phase. The latter gives information about the build-up inside each bunch batch and from batch to batch. In order to obtain this information, the fact that an electron cloud causes a bunch energy loss which can be estimated from the synchronous phase is used. The proton beam circulating in the LHC can lose energy due to various effects. The most important ones are: synchrotron radiation, resistive impedance, and the interaction between the beam and the electron cloud. This energy loss is compensated by the RF system by synchronous phase shift. In the absence of acceleration, the synchronous phase shift is

$$\sin \phi_s = \frac{E_{loss}}{eV}, \tag{2.31}$$

where E_{loss} is the energy loss per turn and per particle and V is the amplitude of the RF voltage. Therefore, the synchronous phase can be used to calculate the bunch energy loss and the total beam energy loss. For the main beam energy losses we have that:

- The energy loss per particle due to synchrotron radiation does not depend on the total bunch intensity, but rather on the energy of the particle and its bending radius. So it introduces the same constant phase offset for all bunches.

- The energy loss per particle due to resistive impedance, depends on the bunch intensity and length. If these are similar for all the bunches, the resulting phase offset will also be similar for all bunches, but it can differ from fill to fill depending on the beam parameters and it will also evolve during each fill as the intensity decreases.

- Finally, the energy loss due to the electron cloud depends on the intensity and length of the bunch, and on the separation between bunches and batches. In addition, and most importantly, it depends on the cloud generated by the passage of the previous bunches.

The synchronous phase can be used to infer the energy loss due to the electron cloud, if the offset caused by the other types of losses is removed and, in particular, the build up of the electron cloud from bunch to bunch and from batch to batch. A concise and clear study about the synchronous phase shift is reported in [15].

Chapter 3

Methodology

The simulations reported in this thesis have been performed using the program ECLOUD version 4.b [16, 17] and the newly developed code PyECLOUD [18] to compute electron-cloud build-up and the resulting heat load in the LHC arc. The heat load per arc unit length is found as a weighted average of three independent simulations for dipoles, field-free regions, and quadrupoles according to the cell fraction covered by each type of field (42.9 m, 6.433 m and 4.119 m, respectively, over a total half cell length of 53.452 m).

3.1 Simulations for the LHC nominal operation

We have conducted four sets of simulations for the nominal operation, two of which corresponding to 25-ns and 50-ns bunch spacing, respectively. And two others with a scan of bunch spacing: for different longitudinal profiles. The characteristics of these sets are listed in Table 3.1. The physical parameters which were varied are: the spacing between bunches, the bunch profile, the number of protons per bunch, the secondary-emission yield and the bunch length. The surface parameters assumed in these calculations are summarized in Table 3.2. The filling pattern for simulations with 25-ns bunch spacing was two trains of 72 bunches separated by 8 missing bunches; for simulations of 50-ns bunch spacing we considered two trains of 36 bunches separated by 4 missing bunches. Heat loads quoted always refer to the average over the two trains. The simulation set A corresponds to the nominal LHC values. The set B assumes the same LHC design parameters except for the larger bunch spacing of 50 ns instead of the nominal 25 ns. The sets C and D represent a study of the heat load as a function of the bunch spacing for a longer flat and shorter Gaussian bunch profile, respectively. The two sets of simulations were performed to explore the heat load dependence on the bunch profile.

Table 3.1: Summary of simulations sets for the LHC nominal operation. A value of σ_x and σ_y = 0.3 mm was assumed.

Set	Secondary-emission yield (δ^*_{max})	Bunch spacing (ns)	Number of particles per bunch (N_b)	Bunch profile	rms bunch length (cm)
A	1.1-1.7	25	$2 \times 10^{10} - 18 \times 10^{10}$	Gaussian	7.55
B	1.1-1.7	50	$2 \times 10^{10} - 18 \times 10^{10}$	Gaussian	7.55
C	1.1, 1.3, 1.5, 1.7	5-50	$6 \times 10^{10} - 2.3 \times 10^{11}$	Flat	11.8
D	1.1, 1.3, 1.5, 1.7	5-50	$6 \times 10^{10} - 2.3 \times 10^{11}$	Gaussian	7.55

Table 3.2: Surface parameters used for the nominal operation of the LHC. the parameter n'_e denotes the rate of primary photoelectrons emitted per proton per meter at 7 TeV beam energy, and Y^* is the associated photoemission yield per absorbed photon.

δ^*_{max}	$\varepsilon^*_{\text{max}}$	n'_e [eV]	Y^* [e/(abs)γ]
1.1	230.0	5.80×10^{-4}	0.025
1.2	232.4	6.53×10^{-4}	0.028
1.3	234.7	7.25×10^{-4}	0.031
1.4	237.1	7.98×10^{-4}	0.034
1.5	239.5	8.71×10^{-4}	0.037
1.6	241.9	9.43×10^{-4}	0.041
1.7	244.2	1.02×10^{-3}	0.044

3.2 Heat-load benchmarking for the cold arcs

Another simulation set (called E from now on) was launched in order to determine the multipacting thresholds at injection and half-top energy (3.5 TeV) for 50 ns bunch spacing. For this set we used the simulation parameters shown in Table 3.3 and a filling pattern consisting of eight batches of 36 bunches each, with a batch spacing of 2.125 μs. All the simulations were performed for a Gaussian bunch profile. During the scrubbing run in 2011 at 50 ns bunch spacing, an important electron cloud related heat load was measured. This motivated a second set of simulations (set F) at 3.5 TeV beam energy, with the same parameters as for the previous one (see Table 3.3). In addition, for this set we changed the filling scheme in order to simulate the bunch filling pattern from LHC fill No. 1704 (pattern used in the LHC on 13/04/2011), for both beams: 228 bunches per beam with an average intensity of 1.22×10^{11} protons per bunch. We omitted the pilot bunches and the small intermediate 12-bunch batches, which are not expected to contribute to the electron-cloud build-up, and we simulated the last six batches of 36 bunches each (216 bunches in total). Between the two batches of a pair there was a spacing of 225 ns (in the simulations 200 ns have been considered due to computational limitations) and between pairs a spacing of 1.1 μs. The measured data per half-cell are shown in Fig. 3.1. To obtain the total electron-cloud heat load per beam and per meter, the values shown have to be divided by about a factor of 100 (the length of a cell). From Fig. 3.1, the average heat load due to the electron cloud (which depends on location) was of the order of 40-50 mW/m/beam. The measurement resolution is estimated to be about 5-10 mW/m/beam. A third set of simulations (set G) was executed in order to benchmark simulations against a measured heat-load value of approximately 1 W/m in October 2011 at injection energy of 25 ns bunch spacing. We also included a study of the electron volume density for this case. Again, we used used the parameters listed in Table 3.3 with a slightly different SEY range (1.5 to 2.0). The filling pattern consisted of batches of 72 bunches, with a batch separation of 925 ns. The fourth set of these simulations (set H) was a study of the multipacting thresholds as a function of the low-energy electron reflectivity R and the bunch spacing. In Table 3.4, we list the parameters used. In order to benchmark simulations and measurements we have employed the different sets in order to infer the multipacting thresholds for the different situations and to generate contour plots that allow us to pin down the values of δ^*_{max} compatible with the heat-load observations. For copper, values of R between 0.2 and 1.0 can be found in the literature (e.g. [14, 19]). In general, we present a scan over R and the corresponding value of δ^*_{max}. However, taking into account measurements for an LHC dipole chamber prototype [19, 20], we then consider a fixed value $R = 0.5$ to estimate the heat load in the LHC arcs and to pin down the corresponding δ^*_{max} value.

Table 3.3: Simulation parameters for sets E, F and G (for F only an energy of 3.5 TeV with 50-ns bunch spacing is considered, whereas for G only injection energy with 25-ns bunch spacing is simulated).

Parameter	450 GeV	3.5 TeV
Bunch intensity (10^{11} ppb)	1.1	1.2
Primary photoelectron emission yield	...	1.233×10^{-4}
Bunch length (cm)	11.8	9
σ_x, σ_y (mm)	1.2	0.3
Pressure (mbar)	4.3×10^{-8}	...

Table 3.4: Summary of simulation parameters for set H.

Parameter	3.5 TeV		
Bunch intensity (ppb)	1.15×10^{11}		
δ^*_{max}	$1.0 - 3.0$		
Primary photoelectron emission yield	1.233×10^{-4}		
R	$0.0 - 1.0$		
Bunch length (cm)	9		
$\sigma_x = \sigma_y$ (mm)	0.3		
Bunch spacing (ns)	25	50	75
Number of bunches per batch	72	36	24
Batch spacing (ns)	200	200	225

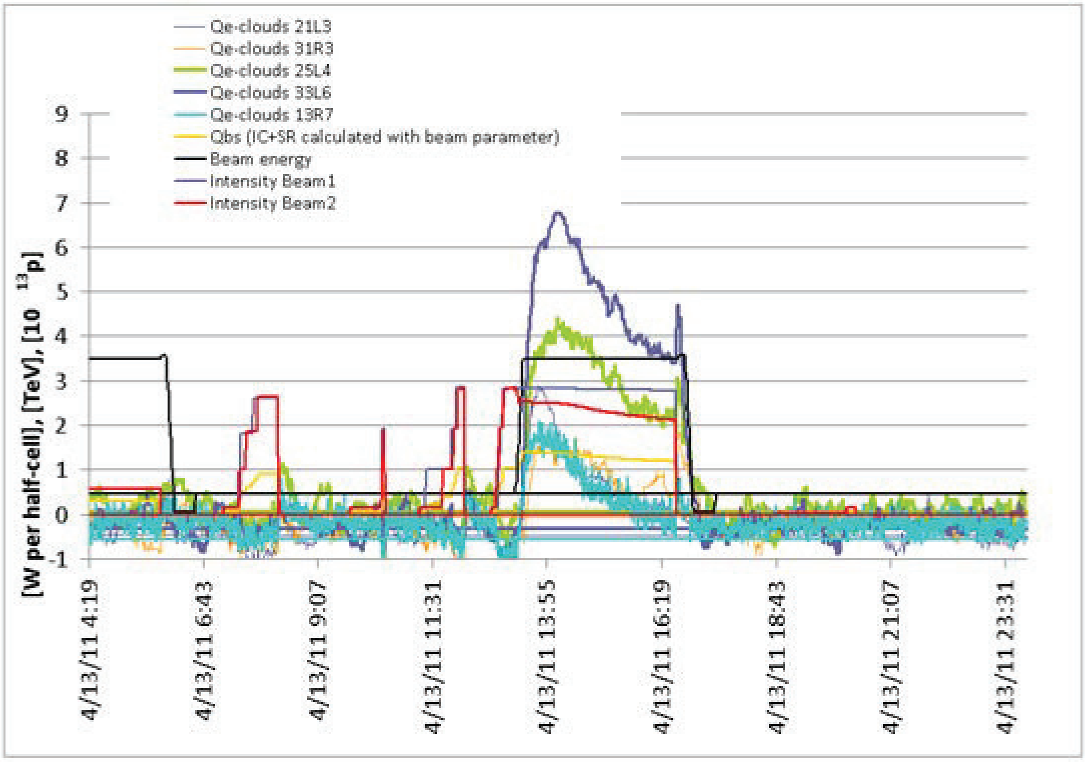

Figure 3.1: Measured heat load due to the electron cloud during the scrubbing process at 50 ns at a beam energy of 3.5 TeV on 13 April 2011. Qbs refers to the computed heat load on the beam screen due to image currents and synchrotron radiation, whereas $Qe-clouds$ are the heat loads associated with electron cloud in different locations, obtained by subtracting Qbs from the measured values.

3.2.1 benchmarking at 25 ns and 4 TeV

The last set of simulations, I, was performed in order to benchmark the cryogenic measurements from the last MD session between 6-10 December 2012. Studies with 25-ns beams at injection energy were done in order to reduce the secondary emission yield (δ^*_{max}) to the lowest value reachable before the long shutdown 1. Eventually, the 25-ns beams were ramped to 4 TeV. Table 3.5 summarizes the simulation parameters employed in this simulation (More details about the fill patterns can be found at [21]). The simulations parameters are the same listed on Table 3.4. In Fig. 3.2 shows some of the cryogenic measures used for this case. Only dipoles were considered.

Table 3.5: Simulation parameters for set I.

Fill number	Fill pattern	Bunch intensity	Bunches
3425	25ns_84b_72_0_0_BBMD1	1.1×10^{11}	84
3427	25ns_156b_72_72_72_BBMD2	1.2×10^{11}	156
3428	25ns_372_72bpi_6inj_2012_MD	1.1×10^{11}	372
3429	25ns_804b_72bpi_12inj_2012_MD	1.06×10^{11}	804
3436	25ns_804b_72bpi_12inj_2012_MD	9.1×10^{10}	804

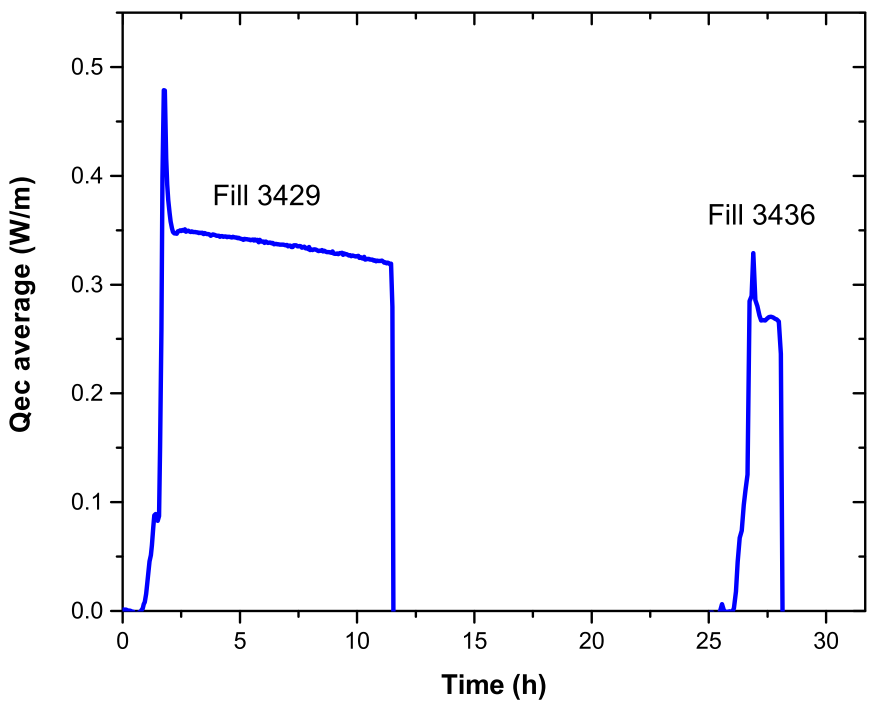

Figure 3.2: Measured heat load due to the electron cloud during the scrubbing process at 25 ns at a beam energy of 4 TeV between 6-10 December 2012, corresponding to the fill numbers 3429 y 3436. *courtesy of Laurent Tavian (CERN).*

Chapter 4

Results

4.1 Introduction

In the following sections, we will present the main results. These results were obtained as described from the simulations of Chapter 3. The low-energy electron reflectivity R is taken to be equal 0.5, unless noted otherwise.

4.2 Heat load for the nominal operation of the LHC

In Fig. 4.1, we can find the heat load values due to the electron cloud for the nominal operation of the LHC. Figure 4.2 shows the results for a larger bunch spacing of 50 ns. As illustrated in Fig. 4.1 the heat load depends on the maximum secondary-emission yield (δ^*_{max}) and on the number of particles per bunch N_b. For certain combinations of (δ^*_{max}) and N_b, the average heat load stays within the available cooling capacity, but for higher values of either (δ^*_{max}) or N_b the average heat is well above the cooling capacity limit. In particular, for reaching the nominal LHC bunch intensity of $N_b = 1.15 \times 10^{11}$ with 25 ns spacing between bunches the maximum secondary-emission yield (δ^*_{max}) should stay below 1.4, which should be readily achieved [22], while for reaching the ultimate bunch intensity of 1.7×10^{11} protons, δ^*_{max} must be smaller than 1.3, which is close to the edge of what appears possible with beam scrubbing. These results are consistent with the previous findings of Furman and Chaplin [23], where, for equivalent model assumptions (i.e., when neglecting the rediffused electrons), almost identical heat-load values to those reported on this thesis were obtained, using the electron-cloud simulation code POSINST. The simulation data for 50-ns bunch spacing are compiled in Fig. 4.2. The average heat load is well below the cooling capacity for any δ^*_{max} value and N_b explored. In fact, the maximum simulated value of the heat load is 0.25 W/m for a $\delta^*_{max} = 1.7$ and $N_b = 1.8 \times 10^{11}$, which is more than a factor of 2 below the available cooling capacity of 0.55 W/m at that point. A more extent study including simulations for the future LHC upgrades scenario can be found at [24].

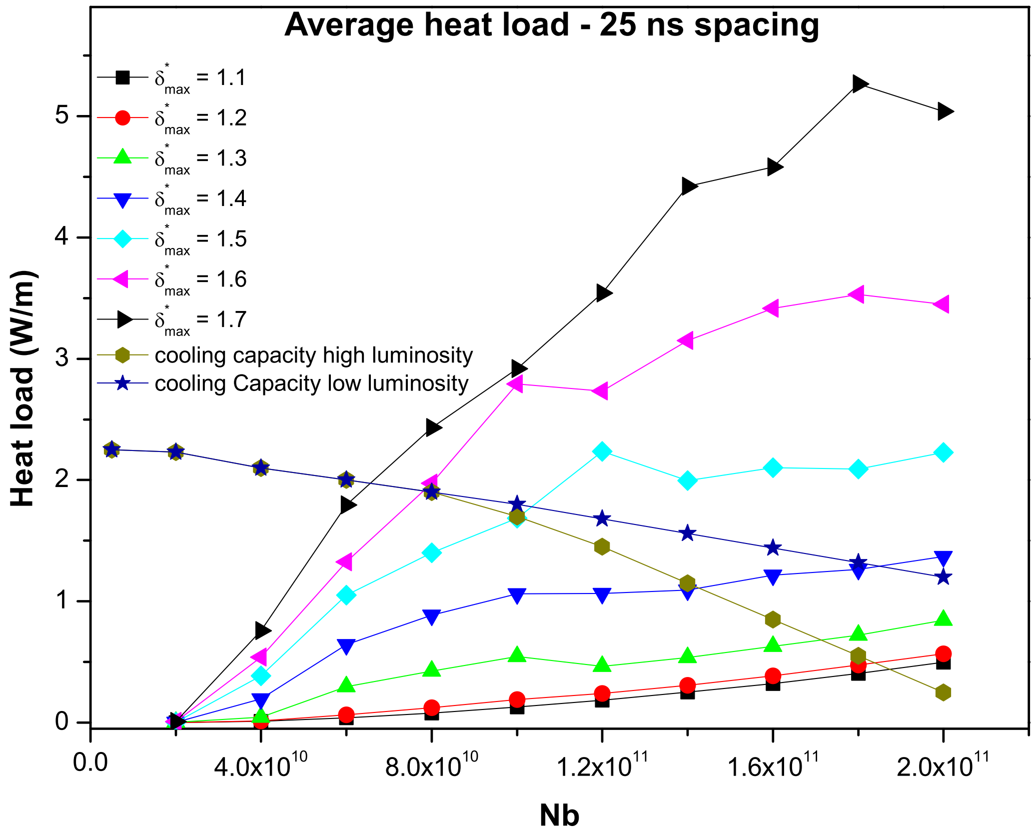

Figure 4.1: Average heat load for the nominal operation of the LHC with 25 ns of bunch spacing.

4.2.1 Variation of bunch spacing

These simulations explored the detailed dependence of the heat load on the bunch spacing and on the longitudinal bunch shape. Results were obtained from the scanning of the bunch spacing for two types of bunch profiles: nominal Gaussian and longer flat bunches. Figure 4.3 shows the results for $\delta^*_{max} = 1.1$ and both types of bunch profiles. Even at this low value of $\delta^*_{max} = 1.1$, the heat load strongly varies with the bunch spacing. The heat load strongly varies with the bunch spacing. The heat load is slightly higher for the Gaussian bunch profile of shorter, nominal bunch length. Finally, Fig. 4.4 presents the results for $\delta^*_{max} = 1.7$, where again the heat load is higher for the nominal Gaussian profile than for the flat one. It is clear that increasing the bunch spacing from 25 to 50 ns is a very efficient mean for mitigating electron-cloud effects in the LHC and its future upgrades.

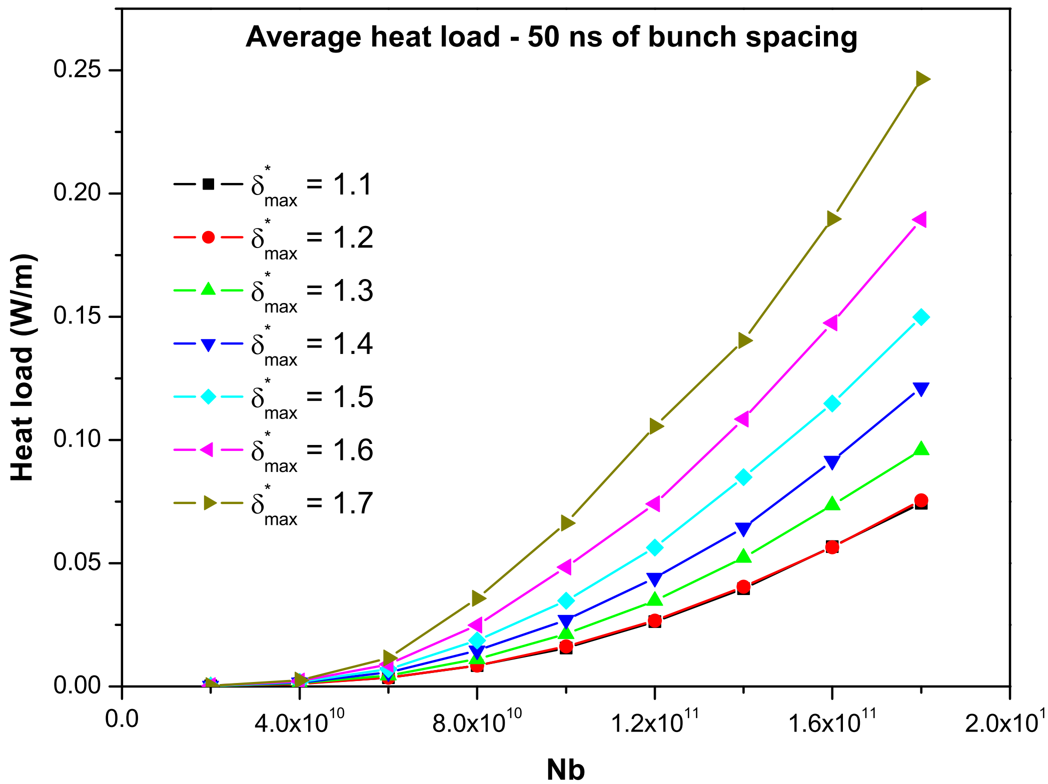

Figure 4.2: Average heat load for the nominal operation of the LHC with 50 ns of bunch spacing.

4.3 Heat-load benchmarking for the cold arcs

Table 4.1 shows the multipacting thresholds found from the simulations of set E and set F. We notice that there is not a very big difference in the thresholds between the 450 GeV injection energy and 3.5 TeV beam energy, except for a slightly earlier start of multipacting for the higher energy. We observe a certain correlation between the reflectivity R and the multipacting thresholds (i.e. increasing R by 0.1 the δ^*_{max} thresholds decrease by the same amount). Figures 4.5 and 4.6 present the heat load obtained for simulation set E (averaged over all the simulated batches). We again remark that the difference between the two beam energies is not dramatic, especially for high δ^*_{max} values. Figure 4.7 shows a contour plot of the heat load for simulation set F (averaged over all six batches). We can infer that to explain the measured heat load of 45 mW/m/beam from 13 April 2011 a maximum secondary-emission yield (δ^*_{max}) slightly above 2.0 is needed. In Fig. 4.8, we show a contour plot of the heat load for the simulation set G (averaged over all the simulated batches). We can see that, in this case, to obtain the measured average heat load around 0.7 W/m from the 25 October 2011 measurements a maximum secondary-emission yield slightly above 1.6 is required.

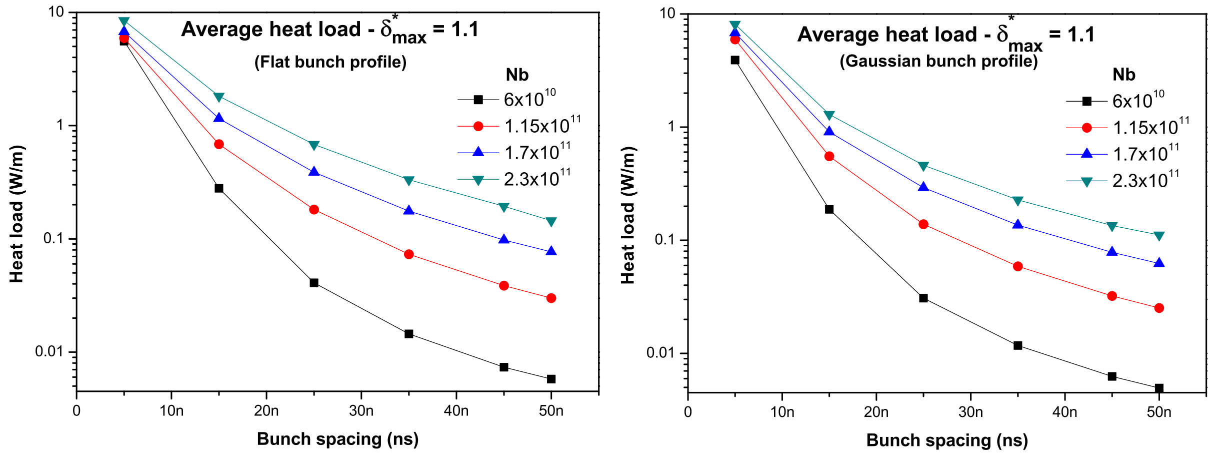

Figure 4.3: Average heat load in function of the bunch spacing and a $\delta^*_{max} = 1.1$ for (a) flat bunch profile and (b) nominal Gaussian bunch profile.

4.4 LHC conditioning status

In 2010 and 2011 first electron-cloud effects have been observed with proton beams in the LHC. Rapid surface conditioning has allowed reducing the bunch spacing from 150 ns over 75 ns down to 50 ns, already during 2010. In order to reach the design LHC bunch spacing of 25 ns in physics operation, further conditioning of the secondary emission yield is required. Thanks to the benchmarking of heat-load observations against simulations, described in this thesis, we have been able to follow up the evolution of δ^*_{max} in the cold arcs of the LHC. Figure 4.9 summarizes the approximate time evolution of δ^*_{max} in the arc dipoles along with the "warm-warm" transitions regions (see [25] for more detail); the multipacting thresholds for 50-ns and 25-ns bunch spacing are also indicated. The strong scrubbing effect of the 25-ns beam during the machine development (MD) sessions is evident. Only 35 h in total were spent with this beam during the MD session. Without it secondary-emission yield values below the 50-ns threshold could not have been reached. Figure 4.10 shows the calculated multipacting thresholds for different bunch-spacing values in the arc dipoles at 3.5 TeV as a function of the reflectivity. For the 2012/2013 bunch spacing of 50 ns, multipacting no longer occurs if the maximum secondary emission yield δ^*_{max} decreases below about 2.0. This is perfectly consistent with observations in 2012 since no evidence of electron cloud was present anymore for 50 ns runs. At the 25-ns bunch spacing a much lower δ^*_{max} value below 1.3 is required to stop multipacting. This large threshold difference between 25 and 50 ns explains the strong electron-cloud related effects still observed during the MD sessions with the 25-ns bunch spacing, since the current δ^*_{max} value is estimated to be larger, e.g., from our benchmarking of simulations against the measured heat load. Figure 4.11 presents a contour plot of the electron volume density for a dipole section (corresponding to simulation set F described

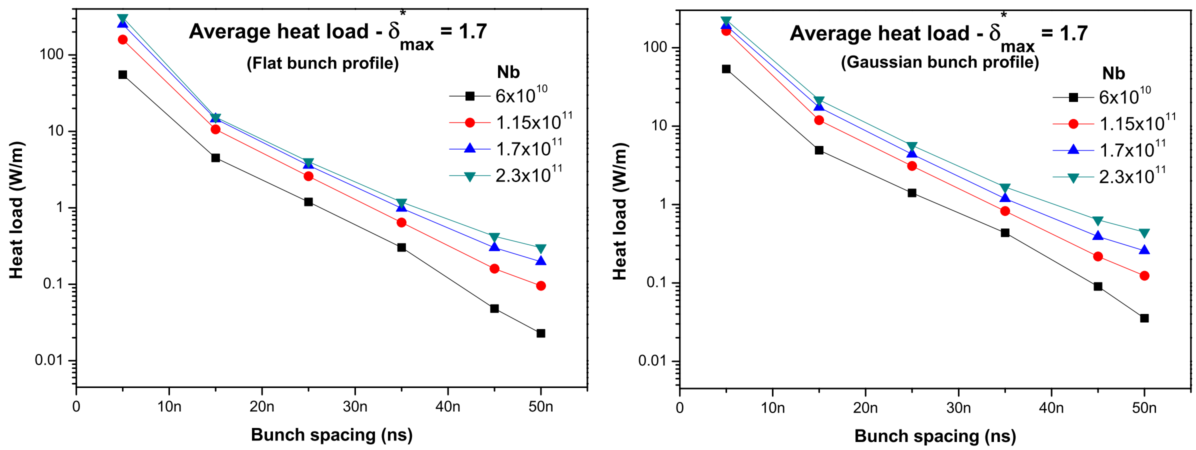

Figure 4.4: Average heat load in function of the bunch spacing and a $\delta^*_{max} = 1.7$ for (a) flat bunch profile and (b) nominal Gaussian bunch profile.

earlier). The (single-bunch) instability threshold for electron cloud in the dipole magnets is around 3×10^{11} m^{-3} [25]. From the figure this means that considering $R \approx 0.5$ we need a $\delta^*_{max} \approx 1.55$ to avoid instabilities. Figure 4.12 shows the raw data from the simulations for the case $R = 0.5$ and $\delta^*_{max} = 1.8$. The central volume density is computed inside a transverse circle of 1-mm radius. Then we plot the average over the total number of simulated bunches. It is clear that further scrubbing is needed to achieve a safe operation parameters for the LHC. In view of this situation, during 2012 the LHC was operated at 50-ns spacing.

4.4.1 LHC last MD studies benchmarking

During the last MD session of 2012, it was possible to ramp the beams up to 4 TeV with a 25-ns bunch spacing. In Fig. 4.13 the simulated heat load is shown. We can observe in order to obtain the measured value of 0.187 W/m/beam a value of $\delta^*_{max} = 1.58$ is needed.

Figure 4.14 shows a contour plot corresponding to the fill number 3429. We can observe that a value of $\delta^*_{max} = 1.54$ is required in order to have the measured heat load of 0.34 W/m/beam.

Finally, from the last measured heat load of 0.27 W/m/beam a value of $\delta^*_{max} = 1.51$ can be inferred from Fig. 4.15.

The secondary emission yield δ^*_{max} time evolution is presented in Fig. 4.16. It can be noted a decrease on δ^*_{max} from 1.58 to 1.51 after around 30 h of beam conditioning.

Table 4.1: Summary of multipacting thresholds for a dipole section of sets A and B (50-ns bunch spacing).

Energy	Reflectivity	δ
450 GeV	0.2	2.4
	0.3	2.3
	0.4	2.2
	0.5	2.1
	0.6	2.0
3.5 TeV	0.2	2.3
	0.3	2.2
	0.4	2.1
	0.5	2.0
	0.6	1.9
	0.7	1.8
	0.8	1.7
	0.9	1.6

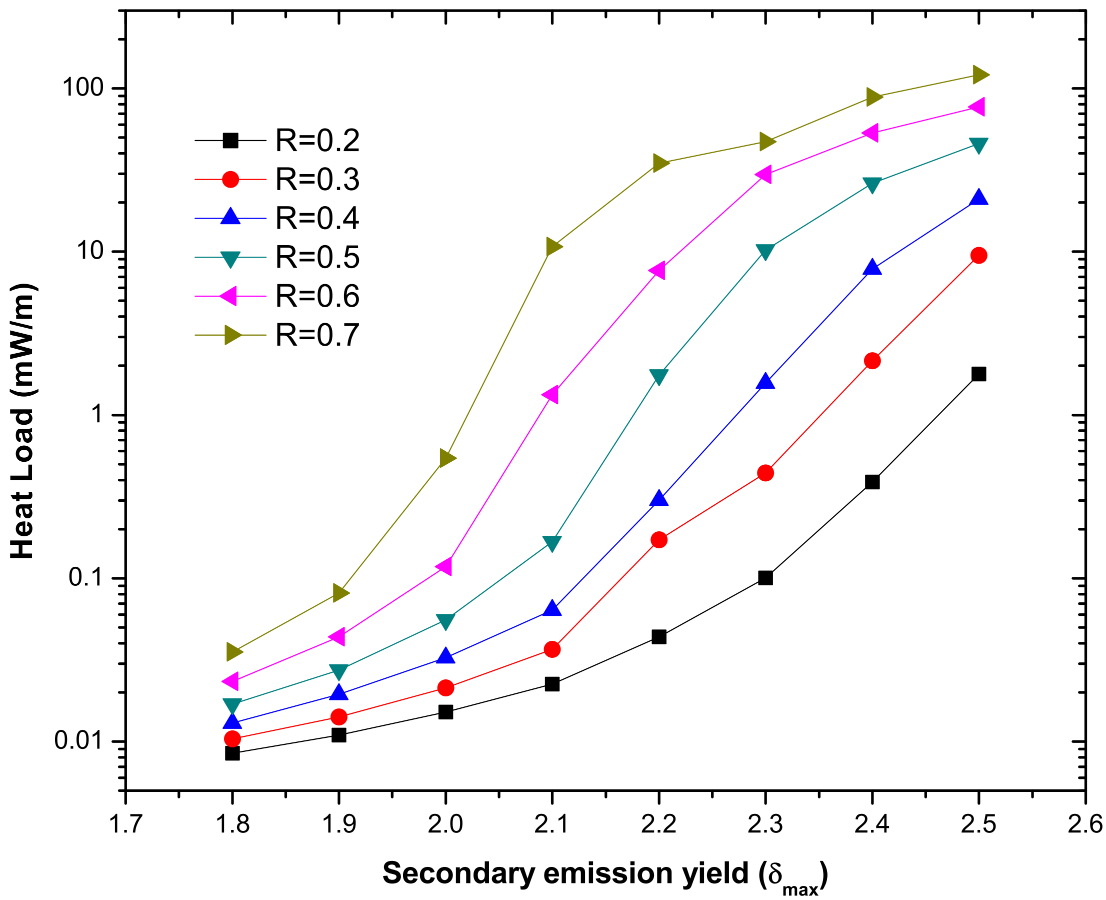

Figure 4.5: Simulated average arc heat load for 50-ns bunch spacing at injection energy. Bunch population: 1.1×10^{11} ppb. During the corresponding experiment, an average heat load of about 20 mW/m was measured.

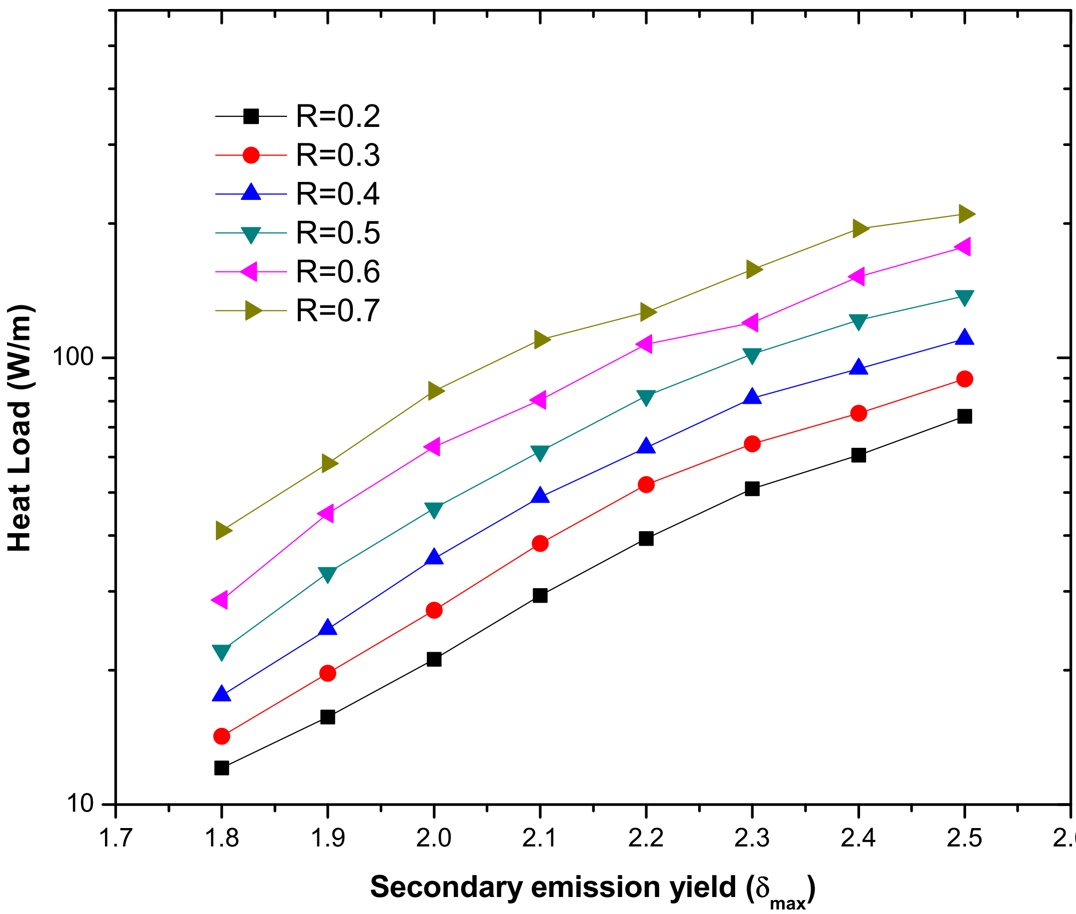

Figure 4.6: Simulated average arc heat load for 50-ns bunch spacing at 3.5 TeV. Bunch population: 1.2×10^{11} ppb. During the corresponding experiment, an average heat load of about 45 mW/m was measured.

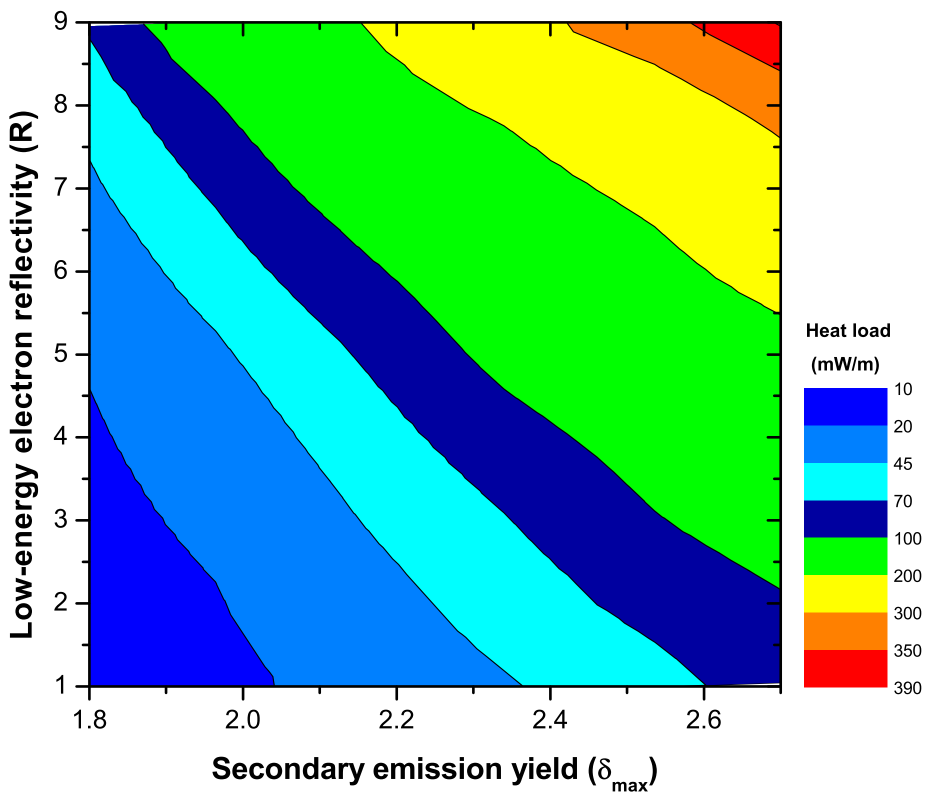

Figure 4.7: Heat-load contour plot for 50-ns bunch spacing at 3.5 TeV beam energy.

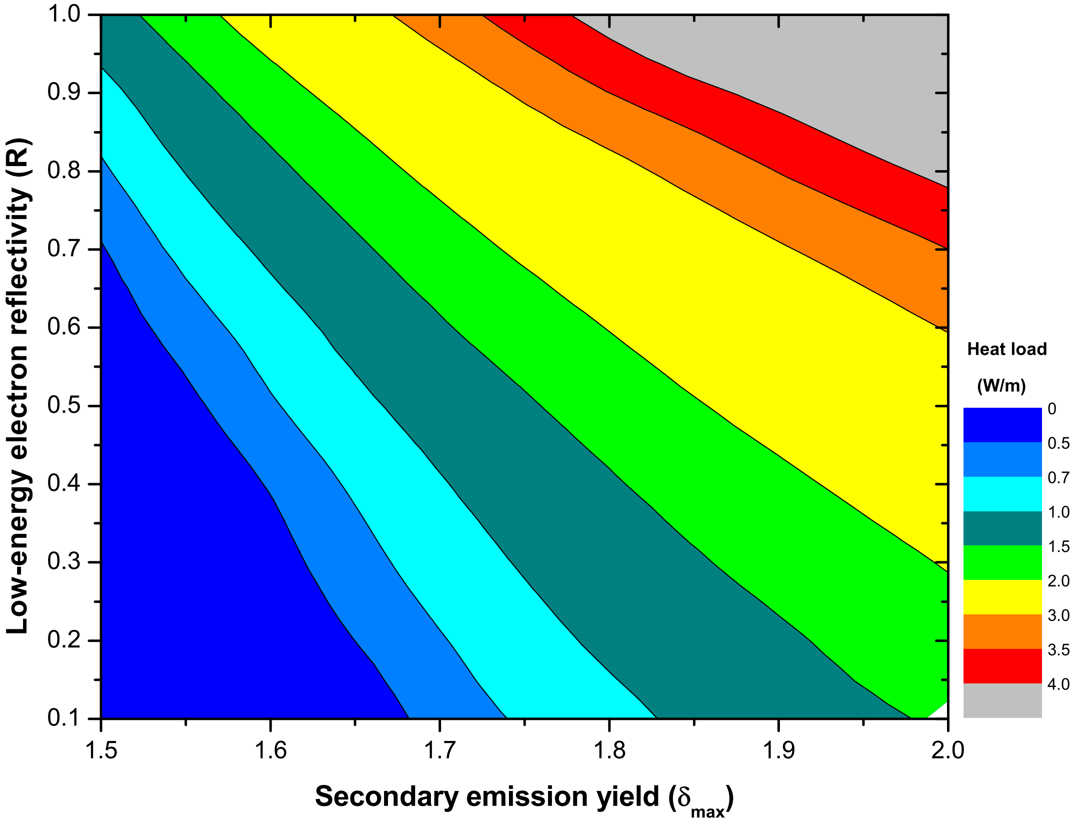

Figure 4.8: Heat-load contour plot for 25-ns bunch spacing at 450 GeV.

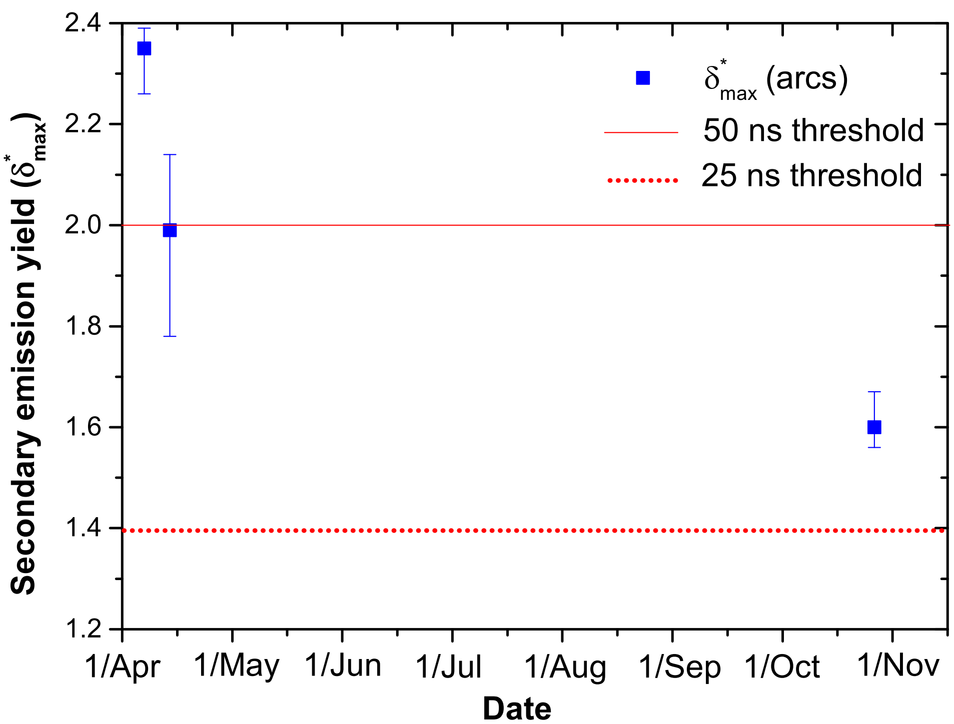

Figure 4.9: Approximate time evolution (from April to October 2011) of δ^*_{max} in the arc dipoles of the LHC.

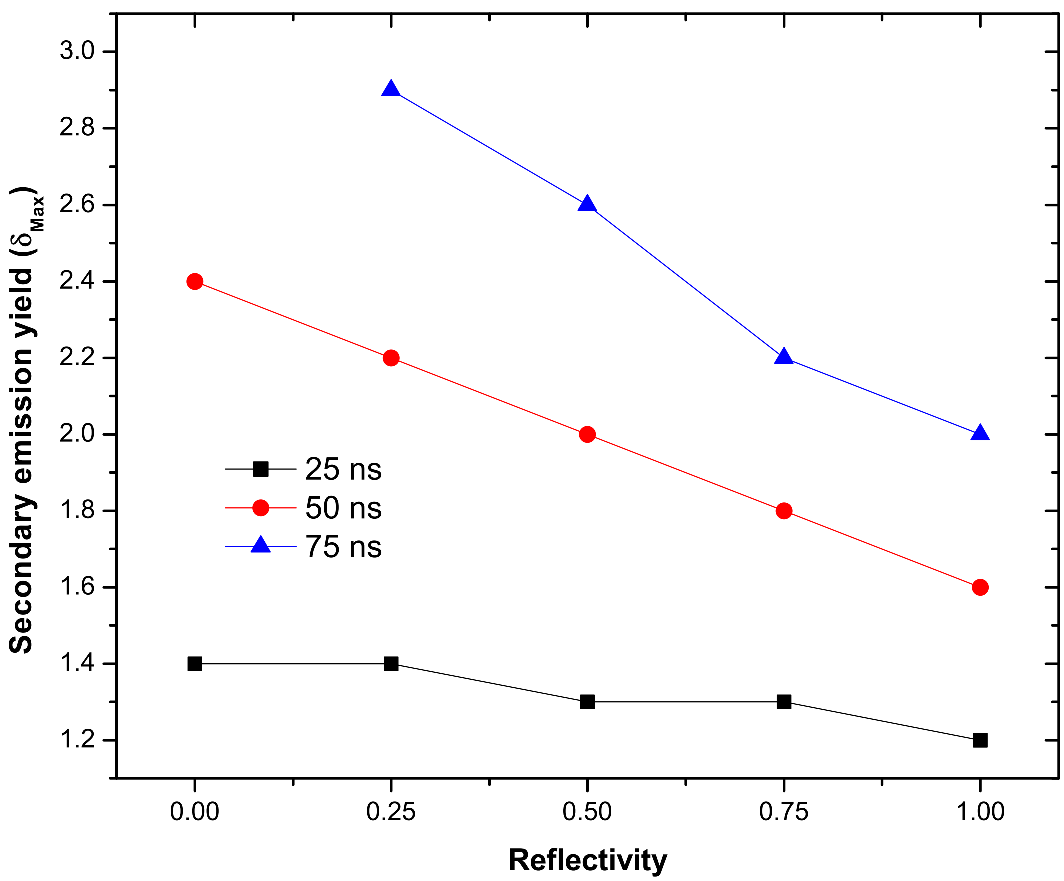

Figure 4.10: Simulated multipacting thresholds for the LHC arc dipoles (chamber half apertures 22×18 mm, magnetic field of 8.33 T, and an intensity of 1.15×10^{11} protons per bunch) as a function of electron reflectivity for three different values of bunch spacing at 3.5 TeV beam energy.

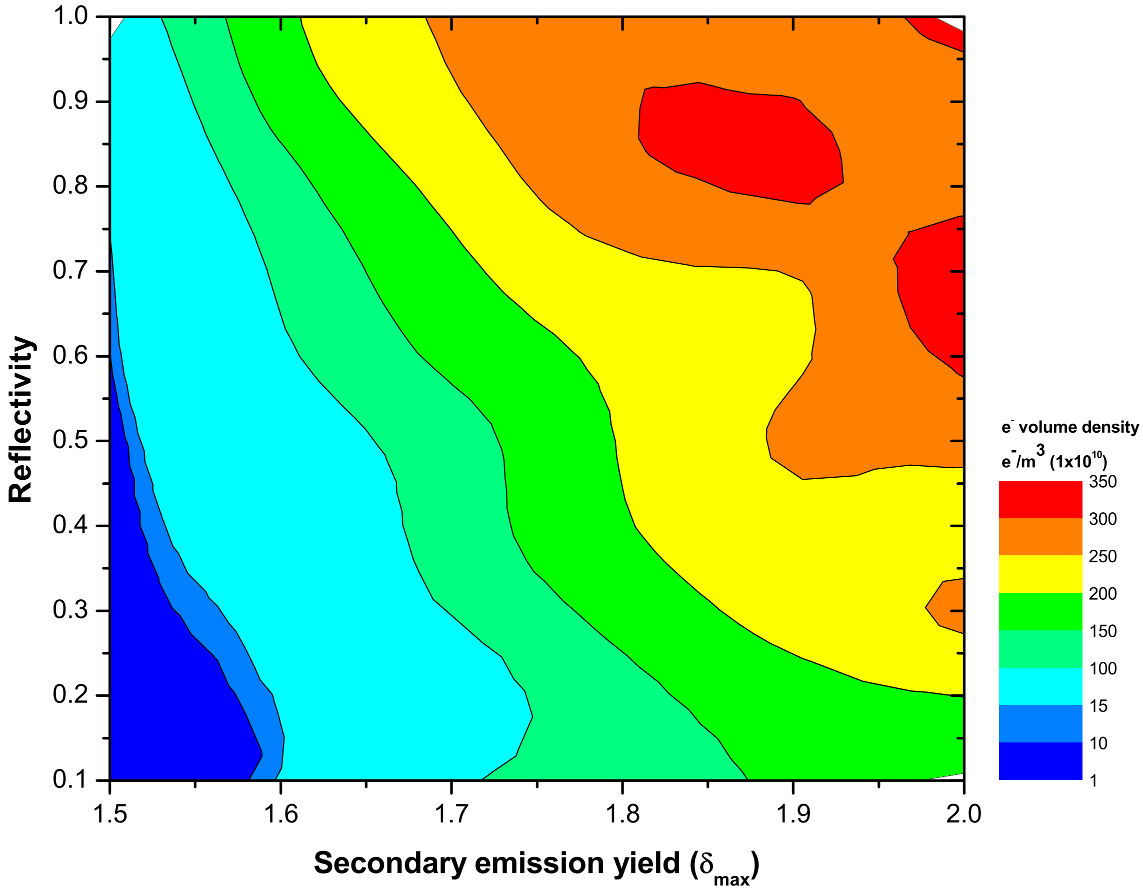

Figure 4.11: Contour plot of the electron volume density in a cylinder of 1 mm radius around the beam in a dipole magnet for the case with 25 ns bunch spacing at injection energy.

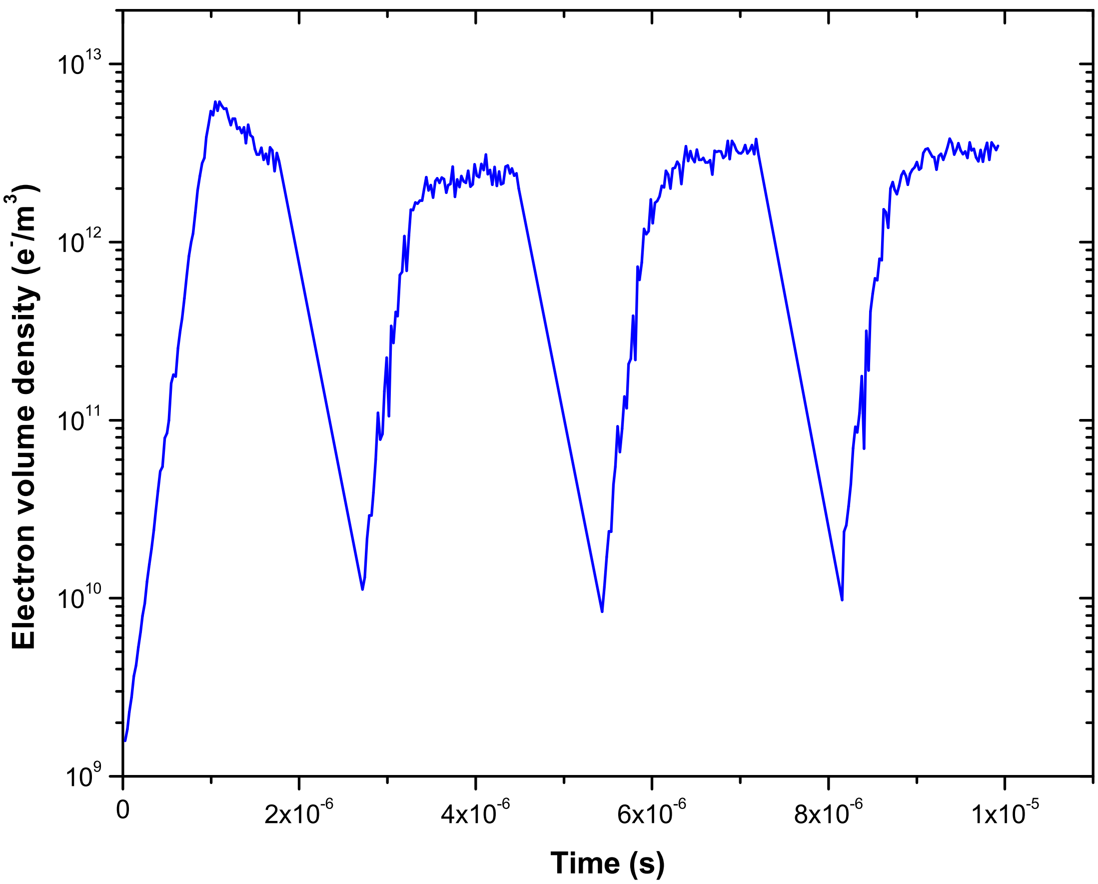

Figure 4.12: Time evolution of the simulated electron volume density (raw simulation data; $R = 0.5$, $\delta^*_{max} = 1.8$).

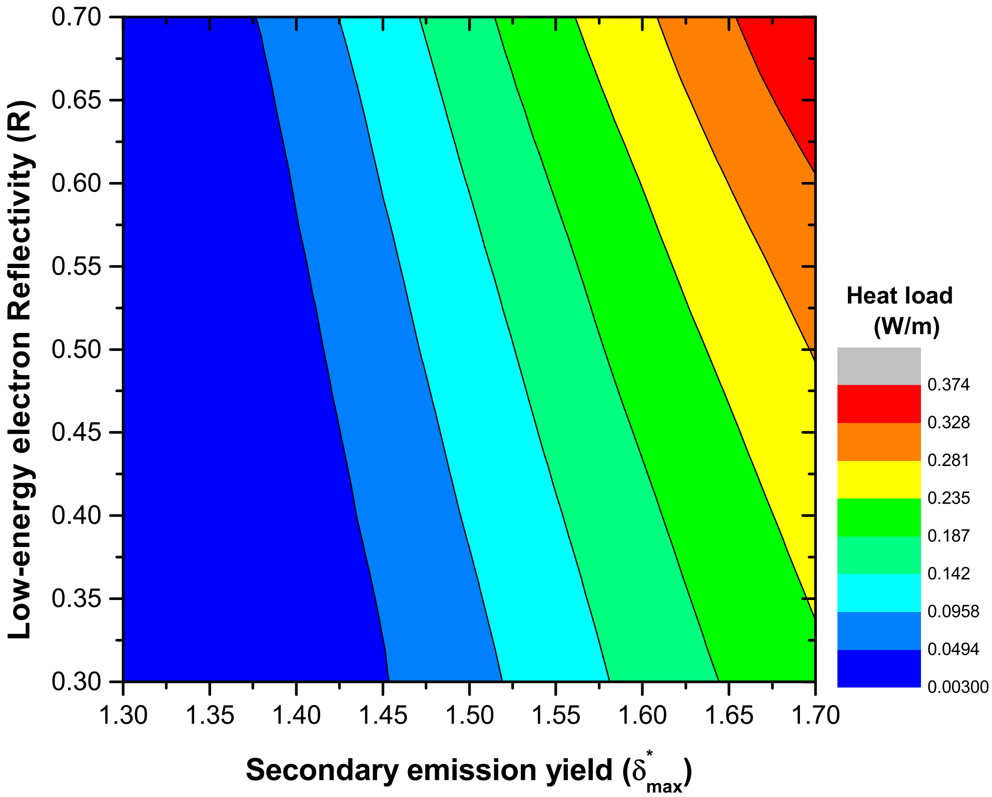

Figure 4.13: Heat-load contour plot for 25-ns bunch spacing at 4 TeV and fill number 3428.

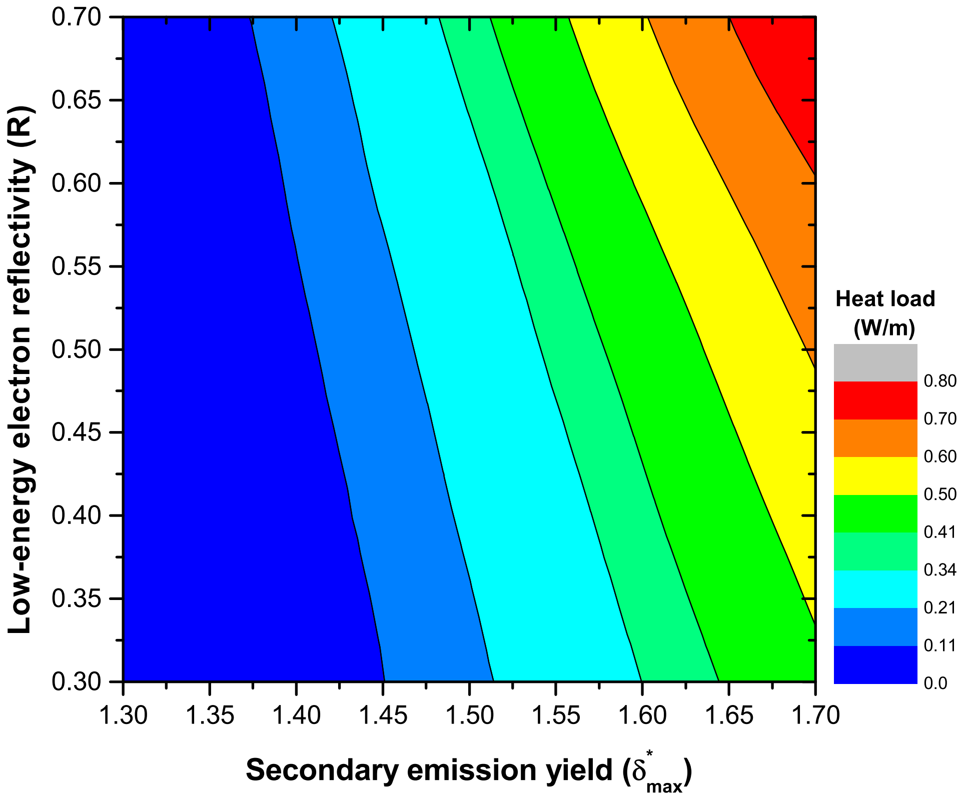

Figure 4.14: Heat-load contour plot for 25-ns bunch spacing at 4 TeV and fill number 3429.

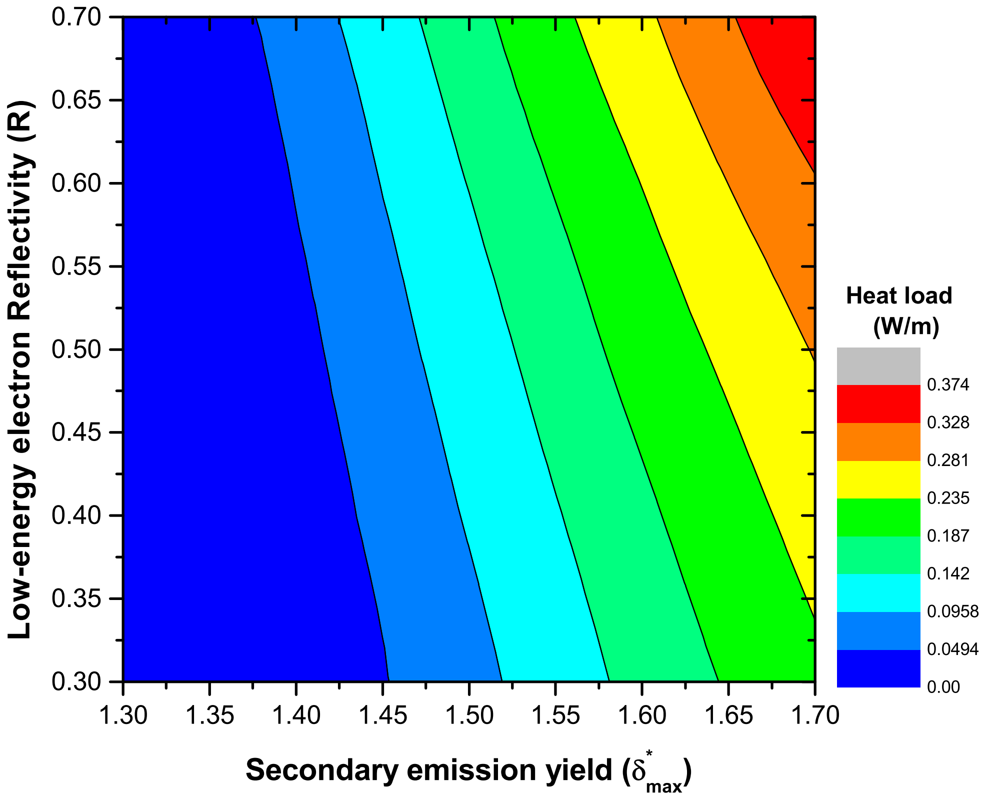

Figure 4.15: Heat-load contour plot for 25-ns bunch spacing at 4 TeV and fill number 3436.

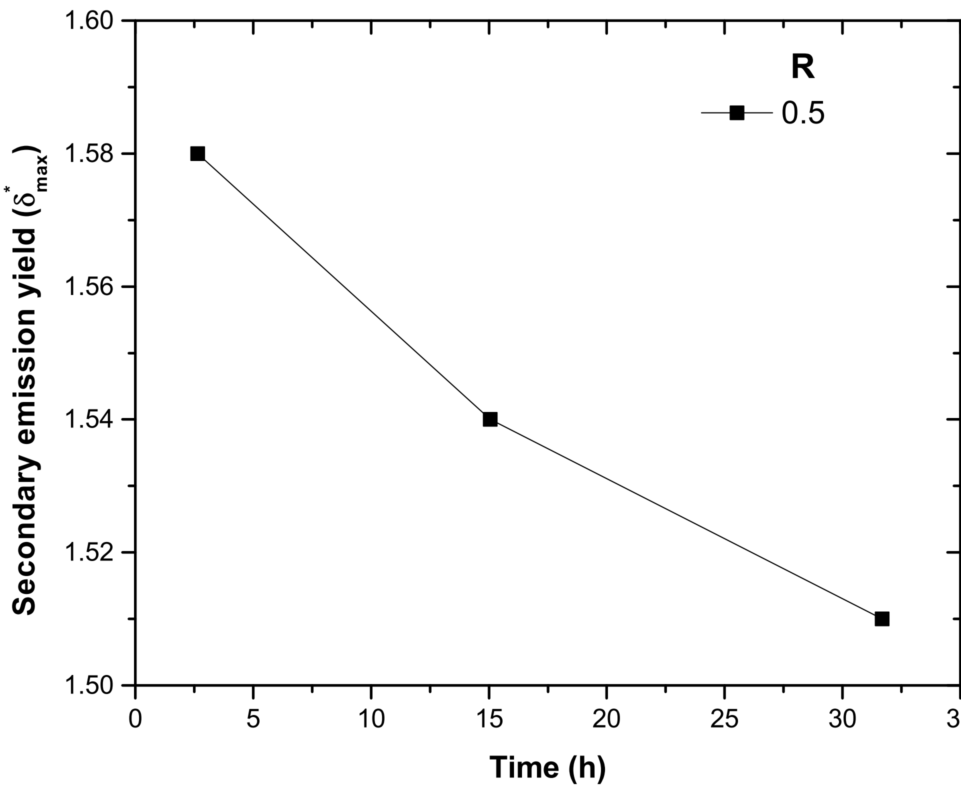

Figure 4.16: Secondary emission yield time evolution during beam conditioning in December 2012.

Conclusions

- For the nominal LHC with 25-ns bunch spacing at top energy, the maximum secondary-emission yield should be below 1.4 in order to reach the nominal bunch intensity $N_b = 1.15 \times 10^{11}$ with acceptable heat load. If the maximum (δ^*_{max}) is higher, between 1.4 and 1.5, bunch population around 10^{11} are still feasible.

- For 50-ns bunch spacing, the electron-cloud build-up is much weaker, and the "nominal" LHC beam -at this, twice the nominal bunch spacing- gives rise to heat loads which remain acceptable up to bunch intensities of 2×10^{11}, without any upgrade to the LHC cryogenics infrastructure.

- The electron-cloud heat load in the LHC strongly depends on the bunch spacing: 50 ns instead of 25 ns looks "safe" up to bunch populations above 4×10^{11}, e.g., roughly 4 times the nominal. For any bunch spacing, additional margins, both in the predicted heat load and especially in the available cooling capacity, can be obtained by operating with longer and flat bunches, instead of nominal Gaussian ones.

- Various types of electron-cloud effects have been observed in the LHC for bunch spacings of 150 ns or below. The effects get much stronger for closer distances between bunches, but fast surface conditioning in 2010 and 2011 made it possible to operate, in 2012, at a bunch spacing of 50 ns (twice the nominal one) without any significant perturbation from electron cloud. The observable considered in this work, namely the heat load deposited on the beam screen inside the cold magnets by the incident electron cloud,it is directly measured by the cryogenics system (through the induced temperature increase of the helium passing through the beam-screen cooling tubes).

- In the cold arcs the observed heat loads can be benchmarked against the simulated energy deposition, showing a reduction of the secondary-emission yield, in the arcs, from an initial value for the maximum secondary-emission yield of about 2.3 town to about 1.6, assuming $R \approx 0.5$, as was shown in Fig. 4.9.

- During the last MD session of 2012 it was observed a small reduction of the secondary emission yield to 1.51.

- The results presented in this thesis can be used, in the future, to quickly estimate actual vacuum-chamber surface parameters (δ^*_{max} and R) from heat-load observations, as well as to predict heat loads in the cold arcs (see Fig 4.10) for a given set of surface parameters.

- Summarizing, significant heat load due to the electron cloud has been observed in the LHC. It is well reproduced in simulations, which can be used to infer the relevant surface parameters and to monitor the progress of beam conditioning.

- It is not yet clear whether further conditioning will be sufficient for the LHC to operate for physics with the nominal 25-ns bunch spacing at near-design energy in the 2015 LHC run. In case of persistent problems with electron clouds at 25 ns, operation with 50 ns remains a fall-back solution.

Future work

- After the long shutdown 1 of the LHC, it will be necessary to repeat the scrubbing run to recover good surface conditions and the low secondary-emission yield from before the shutdown. Future studies, after the LHC restart in 2015 are scheduled to monitor the newer conditions of the LHC surface conditioning.

- The electron cloud effects in the LHC quadrupoles should be studied using the newly developed code PyECLOUD

- The photon distribution along the LHC ring has become a key input for the codes used in the present thesis. Simulations using the code SYNRAD3D are being performed and results for the LHC are expected to be available before the end of 2013.

Bibliography

[1] L. Evans, *The Large Hadron Collider: a marvel of technology*. Fundamental Sciences, Lausanne: EPFL Press, 2009.

[2] H. Maury Cuna and F. Zimmermann, "Electron cloud with inverted beam screens," Tech. Rep. CERN-ATS-Note-2011-129 TECH, 2011.

[3] F. Zimmermann, "A simulation study of electron-cloud instability and beam-induced multipacting in the lhc," Tech. Rep. LHC-Project-Report-95. CERN-LHC-Project-Report-95. SLAC-PUB-7425, CERN, Geneva, Feb 1997.

[4] O. Brüning, "Simulations for the beam-induced electron cloud in the lhc beam screen with magnetic field and image charges. oai:cds.cern.ch:340501," Tech. Rep. LHC-Project-Report-158. CERN-LHC-Project-Report-158, CERN, Geneva, Nov 1997.

[5] G. Stupakov, "Photoelectrons and multipacting in the lhc: Electron cloud build-up. oai:cds.cern.ch:338922," Tech. Rep. LHC-Project-Report-141. CERN-LHC-Project-Report-141, CERN, Geneva, Oct 1997.

[6] L. Vos, "Electron cloud: an analytic view," Tech. Rep. LHC-PROJECT-NOTE-150, CERN, Geneva, Jul 1998.

[7] L. Vos, "Analysis of electron cloud. oai:cds.cern.ch:627584," Tech. Rep. CERN-AB-2003-074-ABP, CERN, Geneva, Jun 2003.

[8] G. Guignard, *Selection of formulae concerning proton storage rings*. Geneva: CERN, 1977.

[9] W. B. Nottingham, W. P. Allis, R. H. Good, R. Kollath, P. F. Little, and L. B. Loeb, *Handbuch der Physik*. Berlin: Springer, 1956.

[10] M. A. Furman and G. R. Lambertson, "The electron-cloud instability in the arcs of the pep-ii positron ring," in *International Workshop on Multibunch Instabilities in Future Electron and Positron Accelerators (MBI'97)* (Y. H. Chin, ed.), p. 170, Dec 1997.

[11] R. Kirby and F. King, "Secondary electron emission yields from pep-ii accelerator materials," *Nuclear Instruments and Methods in Physics Research Section A: Accelerators, Spectrometers, Detectors and Associated Equipment*, vol. 469, no. 1, pp. 1 – 12, 2001.

[12] B. Henrist, N. Hilleret, M. Jiménez, C. Scheuerlein, M. Taborelli, and G. Vorlaufer, "Secondary electron emission data for the simulation of electron cloud," in *Mini-Workshop on Electron Cloud Simulations for Proton and Positron Beams (ECLOUD'02)*, no. CERN-2002-001, p. 75, 2002.

[13] B. Henrist, N. Hilleret, M. Jiménez, C. Scheuerlein, M. Taborelli, and G. Vorlaufer, "The variation of the secondary electron emission with surface modifications." At the Mini-Workshop on Electron Cloud Simulations for Proton and Positron Beams (ECLOUD'02), 2002. [`http://conf-ecloud02.web.cern.ch/conf-ecloud02/talks/hilleret.pdf`].

[14] R. Cimino, I. R. Collins, M. A. Furman, M. Pivi, F. Ruggiero, G. Rumolo, and F. Zimmermann, "Can low-energy electrons affect high-energy physics accelerators?," *Phys. Rev. Lett.*, vol. 93, p. 014801, Jun 2004.

[15] J. F. E. Müller, P. Baudrenghien, G. Iadarola, T. Mastoridis, G. Papotti, G. Rumolo, E. Shaposhnikova, and D. Valuch, "Synchronous phase shift at lhc," p. 8 p, Jun 2013. Comments: Presented at ECLOUD'12: Joint INFN-CERN-EuCARD-AccNet Workshop on Electron-Cloud Effects, La Biodola, Isola d'Elba, Italy, 5-9 June 2012.

[16] G. Rumolo and F. Zimmermann, "Practical user guide for ecloud," Tech. Rep. SL-Note-2002-016-AP, CERN, Geneva, May 2002.

[17] "Ecloud code web site:." [`http://wwwslap.cern.ch/collective/electron-cloud/Programs/Ecloud/ecloud.html`].

[18] G. Iadarola and G. Rumolo, "Electron cloud simulations with pyecloud," no. EuCARD-CON-2012-019, 2012.

[19] V. Baglin, I. Collins, B. Henrist, N. Hilleret, and G. Vorlaufer, "A summary of main experimental results concerning the secondary electron emission of copper," Tech. Rep. LHC-Project-Report-472. CERN-LHC-Project-Report-472, CERN, Geneva, Aug 2001. revised version number 1 submitted on 2002-06-24 11:29:13.

[20] M. A. Furman and M. T. F. Pivi, "Probabilistic model for the simulation of secondary electron emission," *Phys. Rev. ST Accel. Beams*, vol. 5, p. 124404, Dec 2002.

[21] "Lhc filling schemes web site:." [`http://www.lpc.web.cern.ch/lpc/fillingschemes.htm`].

[22] J. M. Jimenez, G. Arduini, P. Collier, G. Ferioli, B. Henrist, N. Hilleret, L. Jensen, K. Weiss, and F. Zimmermann, "Electron cloud with lhc-type beams in the sps: A review of three years of measurements," p. 13 p, Apr 2003. revised version number 1 submitted on 2003-10-16 10:09:19.

[23] M. A. Furman and V. H. Chaplin, "Update on electron-cloud power deposition for the large hadron collider arc dipoles," *Phys. Rev. ST Accel. Beams*, vol. 9, p. 034403, Mar 2006.

[24] H. Maury Cuna, J. G. Contreras, and F. Zimmermann, "Simulations of electron-cloud heat load for the cold arcs of the cern large hadron collider and its high-luminosity upgrade scenarios," *Phys. Rev. ST Accel. Beams*, vol. 15, p. 051001, May 2012.

[25] O. Domínguez, K. Li, G. Arduini, E. Metral, G. Rumolo, F. Zimmermann, and H. M. Cuna, "First electron-cloud studies at the large hadron collider," *Phys. Rev. ST Accel. Beams*, vol. 16, p. 011003, Jan 2013.

List of Publications

Referred Journals

- ”First electron-cloud studies at the Large Hadron Collider” Domínguez, O., Maury Cuna, H., Li, K., Arduini, G., Metral, E., Rumolo, G., and Zimmermann, F., Phys. Rev. ST Accel. Beams 16, 011003, Jan 2013.
- “Simulations of electron-cloud heat load for the cold arcs of the CERN Large Hadron Collider and its high-luminosity upgrade scenarios” H. Maury Cuna, J.G. Contreras and F. Zimmermann, Phys. Rev. ST Accel. Beams 15, 051001, May 2012.

Proceedings of international conferences, workshops and CERN technical notes (not referred)

- ”Synchrotron-radiation photon distribution for highest energy circular colliders”, G. H. I. Maury Cuna G. Dugan D. Sagan F. Zimmermann, Proceedings of IPAC 2013, Vol., Pag.1340-1342.
- “Simulation of electron-cloud heat load for the cold arcs of the large hadron collider”, G. H. I. Maury Cuna G. Iadarola G. Rumolo F. Zimmermann, Proceedings of IPAC 2012, Vol., Pag.115-117.
- ”Simulation of electron-cloud build-up for the cold archs of the lhc and comparison with measured data”, G. H. I. Maury Cuna G. Arduini G. Rumolo L.J. Tavian F. Zimmermann, Proceedings of IPAC 2011, Vol., Pag.1801-1803.
- ”Electron Cloud with Inverted Beam Screens”. Maury Cuna, H. and Zimmermann, F., CERN-ATS-Note-2011-129 TECH. - 2011. - 6 p.